

Adaptive Mesh Refinement for Two-Phase Viscoelastic Fluid Mixture Models

Bindi M. Nagda¹, Aaron Barrett^{2,*}, Boyce E. Griffith^{3,4}, Aaron L. Fogelson⁵, and Jian Du¹

¹*Department of Mathematical Sciences, Florida Institute of Technology, Melbourne, FL, USA*

²*Department of Mathematics, University of Utah, Salt Lake City, UT, USA*

³*Departments of Mathematics, Applied Physical Sciences, and Biomedical Engineering, University of North Carolina, Chapel Hill, NC, USA*

⁴*Carolina Center for Interdisciplinary Applied Mathematics, University of North Carolina, Chapel Hill, NC, USA*

⁵*Departments of Mathematics and Biomedical Engineering, University of Utah, Salt Lake City, UT, USA*

October 2, 2024

Abstract

Multiphase flows are an important class of fluid flow and their study facilitates the development of diverse applications in industrial, natural and biomedical systems. Simulating such flows requires significant computational resources, making it prudent to devise an adaptive mesh refinement (AMR) method to mitigate this burden. We use a mathematical model that takes a continuum mechanical approach to describe multiphase mixture flows. The resulting system of equations poses numerical challenges due to the presence of multiple non-linear terms and a co-incompressibility condition, while the resulting fluid dynamics necessitate the development of an adaptive mesh refinement technique to accurately capture regions of interest while keeping computational costs low. We present an accurate, robust, and efficient computational method for simulating multiphase mixtures on adaptive grids, and utilize a multigrid solver to precondition the saddle-point system. We demonstrate that the AMR solver asymptotically approaches second order accuracy in L^1 , L^2 and L^∞ norms for all solution variables of the Newtonian and non-Newtonian models. All experiments demonstrate the solver is stable provided the time step size satisfies the imposed CFL condition. The solver can accurately resolve sharp gradients in the solution and, with the multigrid preconditioner, the solver behavior is independent of grid spacing. Our AMR solver offers a major cost savings benefit, providing up to 10x speedup in the numerical experiments presented here, with greater speedup possible depending on the problem set-up.

Keywords: AMR, Multiphase, Geometric Multigrid, Co-incompressibility, Saddle-point System.

1 Introduction

Multiphase flow, which is the simultaneous coupled flow of materials with one or more thermodynamic phases, is ubiquitous in many natural and engineered systems. For example, a large portion of industrial processing units involve multiphase flows, whereby several materials coexist and interact with each other. Perhaps one of the most widespread examples is the fluidized bed, a gas-solid system in which pressurized fluid is pumped into particles resulting in a medium that has fluid-like properties. Fluidized beds have the ability to promote

*To whom correspondence should be addressed; email: barrett@math.utah.edu

high levels of contact between gases and solids, resulting in numerous applications in food processing, thermal power generation, and metallurgy [1]. In the natural world, multiphase flows manifest as dust storms in the atmospheric boundary layer [2], sediment transport within rivers [3], and groundwater transport through porous rock [4]. In biological systems, essential phenomena such as platelet thrombus formation [5], cellular protrusion driven by cytoskeletal-membrane interactions [6], DNA packaging [7], and gastric mucus secretion and storage [8, 9] can be characterized by a two-phase mixture of a polymer network and viscous solvent. These fluid systems are referred to as polyelectrolyte gels and are an important class of multiphase mixtures in which the viscous and elastic properties of the network phase can greatly influence the rheology of the gels.

To simulate multiphase mixture flows, we need a mathematical model to describe how it behaves. A widely accepted analytical framework for obtaining constitutive relations for multiphase flows takes a continuum mechanical approach. This mixture model approach is based on describing each material as a continuum, occupying the same region in space and moving according to its own velocity field [10, 11]. The interacting materials are called "phases" even though they are not different phases of the same material, and the resulting multiphase material is called a mixture. Following continuum mechanics, the stresses of each phase need to be specified, along with relations for the coupling between the phases. A group of models has been proposed on the assumption that a local equilibrium establishes over short spatial length scales. Depending on the choice of constitutive equations that control the degree of coupling between the phases, this model is called the two-phase mixture model [10], the algebraic-slip model [12], the drift-flux model [13], the suspension model [14], the diffusion model [10, 15], or the local-equilibrium model [16]. The two-phase mixture model used in this study follows the mathematical model derived by Ishii [10], who provided a detailed macroscopic formulation for two-phase systems. The model is restricted to co-incompressible materials and the pressure is taken to be the average microscopic pressure under the Eulerian averaging procedure. The model consists of a continuity equation and momentum equations for each phase. Each phase is described by a constitutive equation for the Cauchy stress along with an interfacial drag term arising from the differences in velocity between the two phases.

For multiphase flows that incorporate viscoelasticity, such as those used in thrombus formation [5], extensional points in the flow can lead to sharp gradients in the velocity and stress. In single phase flows, extensional points can lead to unbounded growth in the stress for some fluid models [17]. Recent clotting models [5, 18] use multiphase models to capture both the elasticity and the porosity of the thrombus. These models require spatial resolutions that vary in time as the clot increases in size and potentially embolizes, breaking into several pieces. Further, in arterial simulations, for instance, it is necessary to use large domain sizes to ensure boundary effects do not affect the solution; however, coarse grids can be safely utilized to resolve the inlets and outlets. A similar need for high-resolution grids arises in the study of gastric mucus, particularly when modeling the flow dynamics observed during the secretion of mucus from goblet cells in the stomach lining. The process of mucus polymer swelling or collapsing in response to external stimuli occurs very rapidly and often yields interesting pattern formations. For example, when a blob of hydrated mucus polymers undergoes deswelling, the network may form a shrinking polymer annulus under certain conditions [9, 19], whereby there will be a high concentration of solvent on either side of the ring-like structure. A high resolution grid is therefore required to resolve the sharp change in network distribution and phase velocities across the narrow width of the polymer ring. There also is interest in developing high fidelity models of the stomach and the mucus layer lining the stomach epithelium. These models will aid in identifying the mechanisms through which the mucus layer offers a protective barrier against high stomach acidity, digestive enzymes, bacterial infections and gastric cancer [20, 21, 22]. Since interesting dynamics are localized over the gastric mucus layer, which is only a couple hundred

microns wide, this will necessarily require high resolution over the layer to capture the sharp transitions in velocities, fluid stress, and compositions. Sufficient spatial resolution to fully resolve these flow features can lead to unreasonable computational costs when using a uniform mesh. This drawback motivates the need for an adaptive mesh refinement technique to simulate multiphase flows.

Structured adaptive mesh refinement (AMR) was first developed by Berger and Olinger [23] and Berger and Colella [24] for simulating shock hydrodynamics. Their method utilized block-structured adaptive mesh refinement (SAMR) [25], in which logically rectangular regions are tagged for refinement. Alternatives to SAMR methods include tree based methods, in which the generated grid is described by an octree in three spatial dimensions [26]. Completely unstructured methods [27] allow for greater flexibility in grid generation at the cost of increased complexity in discretizations. This study uses a SAMR infrastructure for the ease of grid generation and the functionality to reuse uniform grid discretizations.

To our knowledge, this is the first work to develop and implement a solver for simulating multiphase mixtures on adaptively refined meshes for both Newtonian and non-Newtonian fluid models. We demonstrate that the AMR multiphase solver yields significant savings in computational cost, while maintaining second order accuracy of all variables. The multiphase materials used in this work are treated as co-incompressible. The co-incompressibility condition gives the system an additional difficulty over a single phase system. In single phase fluids, it is common to use projection-based methods [28, 29, 30], in which the incompressibility constraint is enforced by solving an additional Poisson equation. For methods that solve the full saddle point problem, the resulting linear solver can use preconditioners based on projection methods [31]. For the co-incompressible condition used herein, it remains unclear how to project the velocity fields of individual phases that gives fields consistent with both momentum equations. Therefore, in this work, we adapt and test a geometric multigrid based preconditioner to solve the full saddle point system on an adaptive grid. We demonstrate that the solver can accurately resolve sharp gradients in the solution and that, with the multigrid preconditioner, the solver behavior is independent of grid spacing.

2 Model Equations

In this work, we describe the multiphase material as a mixture of two fluids, the viscous solvent (s) and a viscous or viscoelastic network (n). We describe the model and numerical implementation in terms of the viscoelastic network and we detail the changes required to recover a viscous network. Full details about the derivation of the model can be found in prior works [10, 32, 33, 34]. For the two phases, the variables are the volume fractions of network $\theta_n(\mathbf{x}, t)$ and solvent $\theta_s(\mathbf{x}, t)$, the velocities of the two phases, $\mathbf{u}_n(\mathbf{x}, t)$ and $\mathbf{u}_s(\mathbf{x}, t)$, and the pressure $p(\mathbf{x}, t)$. The dynamics of the two volume fractions are governed by the advection equations

$$\frac{\partial}{\partial t}\theta_n(\mathbf{x}, t) + \nabla \cdot (\theta_n(\mathbf{x}, t)\mathbf{u}_n(\mathbf{x}, t)) = 0, \quad (1)$$

$$\frac{\partial}{\partial t}\theta_s(\mathbf{x}, t) + \nabla \cdot (\theta_s(\mathbf{x}, t)\mathbf{u}_s(\mathbf{x}, t)) = 0. \quad (2)$$

These equations, along with the identity $\theta_n(\mathbf{x}, t) + \theta_s(\mathbf{x}, t) = 1$, yield the volume-averaged incompressibility condition,

$$\nabla \cdot (\theta_n(\mathbf{x}, t)\mathbf{u}_n(\mathbf{x}, t) + \theta_s(\mathbf{x}, t)\mathbf{u}_s(\mathbf{x}, t)) = 0. \quad (3)$$

The conservation of momentum of the two fluids yields

$$\rho \left(\frac{\partial \theta_n(\mathbf{x}, t) \mathbf{u}_n(\mathbf{x}, t)}{\partial t} + \nabla \cdot (\theta_n(\mathbf{x}, t) \mathbf{u}_n(\mathbf{x}, t) \mathbf{u}_n(\mathbf{x}, t)) \right) = -\theta_n(\mathbf{x}, t) \nabla p(\mathbf{x}, t) + \nabla \cdot (\theta_n(\mathbf{x}, t) \boldsymbol{\sigma}_n(\mathbf{x}, t)) \quad (4)$$

$$- \xi \theta_n(\mathbf{x}, t) \theta_s(\mathbf{x}, t) (\mathbf{u}_n(\mathbf{x}, t) - \mathbf{u}_s(\mathbf{x}, t)) + \theta_n(\mathbf{x}, t) \mathbf{f}_n(\mathbf{x}, t),$$

$$\rho \left(\frac{\partial \theta_s(\mathbf{x}, t) \mathbf{u}_s(\mathbf{x}, t)}{\partial t} + \nabla \cdot (\theta_s(\mathbf{x}, t) \mathbf{u}_s(\mathbf{x}, t) \mathbf{u}_s(\mathbf{x}, t)) \right) = -\theta_s(\mathbf{x}, t) \nabla p(\mathbf{x}, t) + \nabla \cdot (\theta_s(\mathbf{x}, t) \boldsymbol{\sigma}_s(\mathbf{x}, t)) \quad (5)$$

$$- \xi \theta_n(\mathbf{x}, t) \theta_s(\mathbf{x}, t) (\mathbf{u}_s(\mathbf{x}, t) - \mathbf{u}_n(\mathbf{x}, t)) + \theta_s(\mathbf{x}, t) \mathbf{f}_s(\mathbf{x}, t),$$

in which ρ is the density of each of the two phases, assumed to be equal, ξ is the drag coefficient for the relative motion between the solvent and network, $\mathbf{f}_n(\mathbf{x}, t)$ and $\mathbf{f}_s(\mathbf{x}, t)$ are body forces applied to the fluids, and $\boldsymbol{\sigma}_n(\mathbf{x}, t)$ and $\boldsymbol{\sigma}_s(\mathbf{x}, t)$ are the network and solvent stress tensors. We assume that the inertial effects are small enough so that we can neglect the convective term $\nabla \cdot (\theta_n(\mathbf{x}, t) \mathbf{u}_n(\mathbf{x}, t) \mathbf{u}_n(\mathbf{x}, t))$ that appears in equations (4) and (5). When treated explicitly, including the convective term in our numerical discretization would not effect the efficacy of the solver, which is the primary purpose of this study. The viscous solvent stress tensor is

$$\boldsymbol{\sigma}_s(\mathbf{x}, t) = \mu_s (\nabla \mathbf{u}_s(\mathbf{x}, t) + \nabla \mathbf{u}_s(\mathbf{x}, t)^T) - \mu_s \nabla \cdot \mathbf{u}_s(\mathbf{x}, t) \mathbb{I}, \quad (6)$$

in which μ_s is the solvent viscosity. We assume the network is a viscoelastic material based on clotting models previously derived [5, 35]. In this case, the total stress consists of a viscous and viscoelastic component

$$\boldsymbol{\sigma}_n(\mathbf{x}, t) = \mu_n^v (\nabla \mathbf{u}_n(\mathbf{x}, t) + \nabla \mathbf{u}_n(\mathbf{x}, t)^T) - \mu_n^v \nabla \cdot \mathbf{u}_n(\mathbf{x}, t) \mathbb{I} + \boldsymbol{\sigma}_{ve}(\mathbf{x}, t), \quad (7)$$

$$\frac{\partial \boldsymbol{\sigma}_{ve}(\mathbf{x}, t)}{\partial t} + \nabla \cdot (\mathbf{u}_n(\mathbf{x}, t) \boldsymbol{\sigma}_{ve}(\mathbf{x}, t)) = \boldsymbol{\sigma}_{ve}(\mathbf{x}, t) \cdot \nabla \mathbf{u}_n(\mathbf{x}, t)^T + \nabla \mathbf{u}_n(\mathbf{x}, t) \cdot \boldsymbol{\sigma}_{ve}(\mathbf{x}, t) - \frac{1}{\lambda} (\boldsymbol{\sigma}_{ve}(\mathbf{x}, t) - z(\mathbf{x}, t) \mathbb{I}), \quad (8)$$

$$\frac{\partial z(\mathbf{x}, t)}{\partial t} + \nabla \cdot (\mathbf{u}_n(\mathbf{x}, t) z(\mathbf{x}, t)) = 0, \quad (9)$$

in which μ_n^v is the viscous contribution to the viscosity of the network phase, λ is the relaxation time of the material, and $\boldsymbol{\sigma}_{ve}(\mathbf{x}, t)$ is the viscoelastic stress tensor. Here, $z(\mathbf{x}, t)$ is a quantity that is proportional to the elastic modulus. We note that this model reduces to a viscous model if $z(\mathbf{x}, t) = 0$.

3 Numerical Implementation

We use a structured adaptive mesh refinement framework to discretize the governing equations. The equations are discretized on a hierarchy of grids consisting of locally refined rectangular patches that are organized into a sequence of levels that contain patches all with the same grid spacing. The computational domain consists of a rectangular box Ω such that the coarsest level is a uniform discretization of Ω using grid spacing $(\Delta x^0, \Delta y^0)$. The different patch levels are defined such that patch level ℓ uses grid spacing $(\Delta x^\ell = \frac{\Delta x^0}{r^\ell}, \Delta y^\ell = \frac{\Delta y^0}{r^\ell})$, in which r^ℓ is the refinement ratio between levels. For notational convenience, we describe the methodology for the case that $r^\ell = r$ is constant among all patch levels, although there is no such restriction in our implementation. We use a staggered grid, in which the velocities $\mathbf{u}_n(\mathbf{x}, t)$ and $\mathbf{u}_s(\mathbf{x}, t)$ are stored at cell faces, and the pressure $p(\mathbf{x}, t)$, volume fraction $\theta_n(\mathbf{x}, t)$, and stress tensor $\boldsymbol{\sigma}_{ve}(\mathbf{x}, t)$ are stored at cell centers. A cell in patch level ℓ is denoted by $c_{i,j}^\ell$. We denote the center of cell $c_{i,j}^\ell$ as $\mathbf{x}_{i,j}^\ell$ and the corresponding left cell face as $\mathbf{x}_{i-\frac{1}{2},j}^\ell$. We require that the space covered by patch level ℓ , which we denote by Ω^ℓ , be properly nested within the next coarser level, $\Omega^\ell \subset \Omega^{\ell-1}$.

Computations using the governing multiphase equations are implemented using open-source libraries written in C++ and FORTRAN. The algorithms for our method are developed using the IBAMR open-source library [36], which is an adaptive and MPI parallelized version of the immersed boundary method. Structured grid components are handled using data structures provided by SAMRAI [37], which offers a framework for block-structured adaptive mesh refinement. The resulting linear systems are solved using Krylov solvers provided by PETSc [38], with custom geometric multigrid preconditioners implemented specifically for this study.

3.1 Coarse-Fine Interface Ghost Cells

Each quantity defined on a grid patch is appended with a layer of ghost cells to allow for succinct definitions of difference stencils. Ghost cells can be of two different types: (1) a ghost cell $c_{i,j}^\ell$ can overlap a cell on a patch in the same patch level, so that $c_{i,j}^\ell \subset \Omega^\ell$, or (2) a ghost cell $c_{i,j}^\ell$ can overlap a cell on a patch in the coarser patch level, so that $c_{i,j}^\ell \subset \Omega^{\ell-1}$. In the first case, we can simply copy the values from the neighboring patch into the ghost cell $c_{i,j}^\ell$. In the second case, we employ a quadratic interpolation scheme that incorporates values from the coarse and fine patches as described by Griffith [39]. For completeness, we describe the method in detail below.

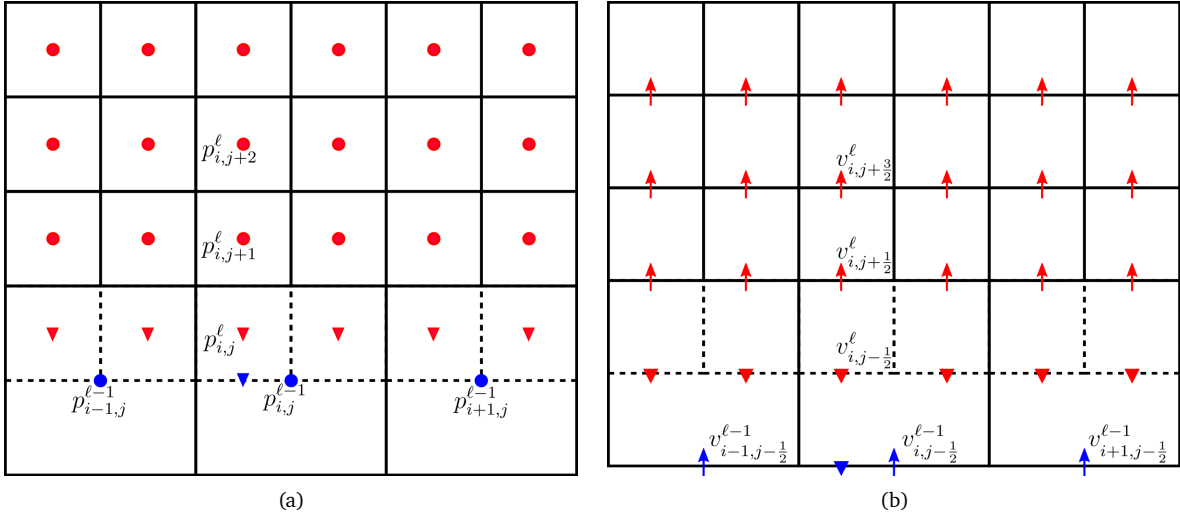


Figure 1: The degree of freedom and coarse-fine interface for cell and side centered grids with a refinement ratio of $r = 2$. Ghost cells are depicted with dashed lines, and values in ghost cells are depicted by red triangles. To compute an approximation to a ghost cell, $p_{i,j}^\ell$ in panel (a) or $v_{i,j-\frac{1}{2}}^\ell$ in panel (b), we first compute a quadratic approximation to the value located at the blue triangle. In this figure the nodes depicted by the blue triangle corresponds to $r = 2$ and $\alpha = 1$. We then compute a quadratic approximation of the ghost cell value using values in the normal direction in the fine patch.

To fill a ghost cell $c_{i,j}^\ell$ such as the one depicted in Figure 1a, for a cell centered quantity $p(\mathbf{x}, t)$, we first quadratically interpolate the coarse values to find the value in line with $c_{i,j}^\ell$ by

$$p_{i-\frac{1}{2}+\frac{\alpha}{r+2},j}^{\ell-1} = \frac{3(r+2)^2 + 4\alpha(r+2) - 4\alpha^2}{4(r+2)^2} p_{i,j}^{\ell-1} + \frac{3(r+2)^2 - 8\alpha(r+2) + 4\alpha^2}{8(r+2)^2} p_{i-1,j}^{\ell-1} - \frac{(r+2)^2 - 4\alpha^2}{8(r+2)^2} p_{i+1,j}^{\ell-1}, \quad (10)$$

in which $\alpha \in \{1, \dots, r+1\}$ refers to the location of the fine cell inside the coarse cell, see Figure 1. We then use

that value along with $p_{i,j+1}^\ell$ and $p_{i,j+2}^\ell$ to obtain

$$p_{i,j}^\ell = p_{i,j+1}^\ell \frac{2r-2}{r+1} + p_{i,j+2}^\ell \frac{1-r}{3+r} + p_{i-\frac{1}{2}+\frac{\alpha}{r+2},j}^{\ell-1} \frac{8}{3+4r+r^2}. \quad (11)$$

For side centered quantities, the component tangential to the patch's coarse-fine boundary is computed using the same interpolation scheme as centered quantities. For the component normal to the patch's coarse-fine boundary, we perform a similar procedure. To compute an approximation to $v_{i,j-\frac{1}{2}}^\ell$ as depicted in Figure 1b, we first quadratically interpolate the coarse values to find an approximation to $v_{i-\frac{1}{2}+\frac{\alpha}{r+2},j-\frac{1}{2}}^{\ell-1}$ by

$$v_{i-\frac{1}{2}+\frac{\alpha}{r+2},j-\frac{1}{2}}^{\ell-1} = \frac{3(r+2)^2 - 8\alpha(r+2) + 4\alpha^2}{8(r+2)^2} v_{i-1,j-\frac{1}{2}}^{\ell-1} + \frac{3(r+2)^2 + 4\alpha(r+2) - 4\alpha^2}{4(r+2)^2} v_{i,j-\frac{1}{2}}^{\ell-1} - \frac{(r+2)^2 - 4\alpha^2}{8(r+2)^2} v_{i+1,j-\frac{1}{2}}^{\ell-1}. \quad (12)$$

We then compute a quadratic approximation to $v_{i,j-\frac{1}{2}}^\ell$ by

$$v_{i,j-\frac{1}{2}}^\ell = \frac{r}{2r+2} v_{i,j+\frac{1}{2}}^\ell + \frac{r}{2r-2} v_{i,j+\frac{3}{2}}^\ell - \frac{1}{r^2-1} v_{i-\frac{1}{2}+\frac{\alpha}{r+2},j-\frac{1}{2}}^{\ell-1}. \quad (13)$$

In locations where we do not have enough data to perform these interpolations, for example, at the corners of the coarse-fine interface, we use linear interpolation from coarse values to fill ghost cells. We note that this leads to first order accuracy in these cells. This reduction in order is localized to corners in the coarse fine interface, which is a set of codimension 2, and, as we will demonstrate, second order accuracy is retained sufficiently far away from the interface.

3.2 Finite Difference Operators

We require finite difference operators for the discrete gradient, discrete divergence, and variable coefficient Laplacian. The cell centered discrete gradient $G_h^{c \rightarrow f}$ acts on cell centered quantities and returns side centered quantities. The discrete divergence $D_h^{f \rightarrow c}$ acts on side centered quantities and returns cell centered quantities. The variable coefficient Laplacian $\Delta_h^{f \rightarrow f}[\theta] = [\Delta_h^{f \rightarrow f}{}_0[\theta], \Delta_h^{f \rightarrow f}{}_1[\theta]]^T$ acts on side quantities and returns side centered quantities. We define the action of the operators for a patch level ℓ and cell $c_{i,j}^\ell$ by

$$\left(G_h^{c \rightarrow f}\right)_{i+\frac{1}{2},j}^\ell = \frac{p_{i+1,j}^\ell - p_{i,j}^\ell}{\Delta x^\ell}, \quad (14)$$

$$\left(D_h^{f \rightarrow c}\right)_{i,j}^\ell = \frac{u_{i+\frac{1}{2},j}^\ell - u_{i-\frac{1}{2},j}^\ell}{\Delta x^\ell} + \frac{v_{i,j+\frac{1}{2}}^\ell - v_{i,j-\frac{1}{2}}^\ell}{\Delta y^\ell}, \quad (15)$$

$$\begin{aligned} \left(\Delta_h^{f \rightarrow f}{}_0[\theta]\right)_{i+\frac{1}{2},j}^\ell &= \frac{1}{\Delta x} \left(\theta_{i+1,j} \frac{u_{i+\frac{3}{2},j} - u_{i+\frac{1}{2},j}}{\Delta x} - \theta_{i,j} \frac{u_{i+\frac{1}{2},j} - u_{i-\frac{1}{2},j}}{\Delta x} \right) \\ &+ \frac{1}{\Delta y} \left(\theta_{i+\frac{1}{2},j+\frac{1}{2}} \frac{u_{i+\frac{1}{2},j+1} - u_{i+\frac{1}{2},j}}{\Delta y} - \theta_{i+\frac{1}{2},j-\frac{1}{2}} \frac{u_{i+\frac{1}{2},j} - u_{i+\frac{1}{2},j-1}}{\Delta y} \right) \\ &+ \frac{1}{\Delta y} \left(\theta_{i+\frac{1}{2},j+\frac{1}{2}} \frac{v_{i+1,j+\frac{1}{2}} - v_{i,j+\frac{1}{2}}}{\Delta x} - \theta_{i+\frac{1}{2},j-\frac{1}{2}} \frac{v_{i+1,j-\frac{1}{2}} - v_{i,j-\frac{1}{2}}}{\Delta x} \right) \\ &- \frac{1}{\Delta x} \left(\theta_{i+1,j} \frac{v_{i+1,j+\frac{1}{2}} - v_{i+1,j-\frac{1}{2}}}{\Delta y} - \theta_{i,j} \frac{v_{i,j+\frac{1}{2}} - v_{i,j-\frac{1}{2}}}{\Delta y} \right), \end{aligned} \quad (16)$$

$$\begin{aligned}
(\Delta_h^{f \rightarrow f} [\theta])_{i,j+\frac{1}{2}}^\ell &= \frac{1}{\Delta y} \left(\theta_{i,j+1} \frac{v_{i,j+\frac{3}{2}} - v_{i,j+\frac{1}{2}}}{\Delta y} - \theta_{i,j} \frac{v_{i,j+\frac{1}{2}} - v_{i,j-\frac{1}{2}}}{\Delta y} \right) \\
&+ \frac{1}{\Delta x} \left(\theta_{i+\frac{1}{2},j+\frac{1}{2}} \frac{v_{i+1,j+\frac{1}{2}} - v_{i,j+\frac{1}{2}}}{\Delta x} - \theta_{i-\frac{1}{2},j+\frac{1}{2}} \frac{(v_{i,j+\frac{1}{2}} - v_{i-1,j+\frac{1}{2}})}{\Delta x} \right) \\
&+ \frac{1}{\Delta x} \left(\theta_{i+\frac{1}{2},j+\frac{1}{2}} \frac{u_{i+\frac{1}{2},j+1} - u_{i+\frac{1}{2},j}}{\Delta y} - \theta_{i-\frac{1}{2},j+\frac{1}{2}} \frac{(u_{i-\frac{1}{2},j+1} - u_{i-\frac{1}{2},j})}{\Delta y} \right) \\
&- \frac{1}{\Delta y} \left(\theta_{i,j+1} \frac{u_{i+\frac{1}{2},j+1} - u_{i-\frac{1}{2},j+1}}{\Delta x} - \theta_{i,j} \frac{(u_{i+\frac{1}{2},j} - u_{i-\frac{1}{2},j})}{\Delta x} \right), \tag{17}
\end{aligned}$$

in which $\theta_{i-\frac{1}{2},j-\frac{1}{2}}$ is the volume fraction interpolated to a cell corner. We perform this interpolation by taking the average of the surrounding cell values, $\theta_{i-\frac{1}{2},j-\frac{1}{2}} = \frac{\theta_{i-1,j-1} + \theta_{i,j-1} + \theta_{i-1,j} + \theta_{i,j}}{4}$. We additionally define an interpolation operator $\mathcal{J}^{c \rightarrow f}$ that interpolates cell centered quantities to cell sides

$$\mathcal{J}^{c \rightarrow f} [\theta_{i,j}] = \left[\theta_{i+\frac{1}{2},j}, \theta_{i,j+\frac{1}{2}} \right]^T = \left[\frac{\theta_{i,j} + \theta_{i+1,j}}{2}, \frac{\theta_{i,j} + \theta_{i,j+1}}{2} \right]^T. \tag{18}$$

This operator acts on scalar quantities and returns staggered vector quantities.

For viscoelastic flows, we require a discrete divergence of the stress tensor D_h^{stress} . This operator is defined by

$$D_h^{\text{stress}} \sigma_{\text{ve},i,j} = \begin{bmatrix} D_h^{\text{stress},0} \\ D_h^{\text{stress},1} \end{bmatrix} \sigma_{\text{ve},i,j}, \tag{19}$$

$$D_h^{\text{stress},0} \sigma_{\text{ve},i,j} = \frac{\sigma_{xx_{i,j}} - \sigma_{xx_{i-1,j}}}{\Delta x} + \frac{\sigma_{xy_{i+1,j+1}} + \sigma_{xy_{i-1,j+1}} - \sigma_{xy_{i+1,j-1}} - \sigma_{xy_{i-1,j-1}}}{4\Delta y}, \tag{20}$$

$$D_h^{\text{stress},1} \sigma_{\text{ve},i,j} = \frac{\sigma_{xy_{i+1,j+1}} + \sigma_{xy_{i+1,j-1}} - \sigma_{xy_{i-1,j+1}} - \sigma_{xy_{i-1,j-1}}}{4\Delta x} + \frac{C_{xx_{i,j}} - C_{xx_{i,j-1}}}{\Delta y}, \tag{21}$$

in which the components of the symmetric tensor σ_{ve} are written as $\sigma_{\text{ve}} = \begin{bmatrix} \sigma_{xx} & \sigma_{xy} \\ \sigma_{xy} & \sigma_{yy} \end{bmatrix}$.

With these operators defined, the momentum and mass equations (3) to (5) are discretized in space, resulting in the algebraic differential equations

$$\rho \frac{d\mathcal{J}^{c \rightarrow f}(\theta_n) \mathbf{u}_n}{dt} = -\mathcal{J}^{c \rightarrow f}(\theta_n) G_h^{c \rightarrow f} p + \mu_n^\nu \Delta_h^{f \rightarrow f} [\theta_n] \mathbf{u}_n + D_h^{\text{stress}} \bar{\tau}_n - \xi \mathcal{J}^{c \rightarrow f}(\theta_n \theta_s) (\mathbf{u}_n - \mathbf{u}_s) \tag{22a}$$

$$\rho \frac{d\mathcal{J}^{c \rightarrow f}(\theta_s) \mathbf{u}_s}{dt} = -\mathcal{J}^{c \rightarrow f}(\theta_s) G_h^{c \rightarrow f} p + \mu_s \Delta_h^{f \rightarrow f} [\theta_s] \mathbf{u}_s - \xi \mathcal{J}^{c \rightarrow f}(\theta_n \theta_s) (\mathbf{u}_s - \mathbf{u}_n), \tag{22b}$$

$$0 = D_h^{f \rightarrow c} \left(\mathcal{J}^{c \rightarrow f}(\theta_n) \mathbf{u}_n \right) + D_h^{f \rightarrow c} \left(\mathcal{J}^{c \rightarrow f}(\theta_s) \mathbf{u}_s \right). \tag{22c}$$

In addition, the transport equation for the network volume fraction given by equation (1) is discretized by

$$\frac{d\theta_n}{dt} = -\mathbf{N} [\mathbf{u}_n, \theta_n], \tag{23}$$

in which $\mathbf{N} [\mathbf{u}_n, \theta_n]$ is an approximation to $\nabla \cdot (\mathbf{u}_n \theta_n)$ using a cubic upwinded interpolation (CUI) scheme [40]. The solvent volume fraction is computed as $\theta_s = 1 - \theta_n$.

For the viscoelastic stress tensor equation, we require stencils for the velocity gradient. These are computed by

$$\nabla_h \mathbf{u} = \begin{bmatrix} \frac{u_{i+\frac{1}{2},j} - u_{i-\frac{1}{2},j}}{\Delta x} & \frac{u_{i+\frac{1}{2},j} + u_{i-\frac{1}{2},j} - u_{i+\frac{1}{2},j-1} - u_{i-\frac{1}{2},j-1}}{4\Delta y} \\ \frac{v_{i+1,j+\frac{1}{2}} + v_{i+1,j-\frac{1}{2}} - v_{i-1,j+\frac{1}{2}} - v_{i-1,j-\frac{1}{2}}}{4\Delta x} & \frac{v_{i,j+\frac{1}{2}} - v_{i,j-\frac{1}{2}}}{\Delta y} \end{bmatrix} \quad (24)$$

in which the components of the velocity are denoted as $\mathbf{u} = [u, v]^T$. The stress tensor and elastic modulus equations given by equations (8) and (9) are therefore discretized as

$$\frac{d\sigma_{ve}}{dt} = \mathbb{F}(\mathbf{u}_n, \sigma_{ve}, z) = -\mathbf{N}[\mathbf{u}_n, \sigma_{ve}] + \sigma_{ve}(\nabla_h \mathbf{u}_n)^T + \nabla_h \mathbf{u}_n \sigma_{ve} - \frac{1}{\lambda}(\sigma_{ve} - z\mathbb{I}), \quad (25)$$

$$\frac{dz}{dt} = -\mathbf{N}[\mathbf{u}_n, z]. \quad (26)$$

3.3 Temporal Discretization

We discretize equation (22) using an implicit trapezoidal rule for the viscous stress and drag and a second order Adams-Bashforth scheme for the transport equations (23) and (25). To advance the solution from time t^k to time $t^{k+1} = t^k + \Delta t$, we first compute θ_n^{k+1} , θ_s^{k+1} , σ_{ve}^{k+1} , and z^{k+1} by

$$\theta_n^{k+1} = \theta_n^k + \Delta t \left(\frac{3}{2} \mathbf{N}[\mathbf{u}_n^k, \theta_n^k] - \frac{1}{2} \mathbf{N}[\mathbf{u}_n^{k-1}, \theta_n^{k-1}] \right), \quad (27)$$

$$\theta_s^{k+1} = 1 - \theta_n^{k+1}, \quad (28)$$

$$\sigma_{ve}^{k+1} = \sigma_{ve}^k + \Delta t \left(\frac{3}{2} \mathbb{F}(\mathbf{u}_n^k, \sigma_{ve}^k, z^k) - \frac{1}{2} \mathbb{F}(\mathbf{u}_n^{k-1}, \sigma_{ve}^{k-1}, z^{k-1}) \right), \quad (29)$$

$$z^{k+1} = z^k - \Delta t \left(\frac{3}{2} \mathbf{N}[\mathbf{u}_n^k, z^k] - \frac{1}{2} \mathbf{N}[\mathbf{u}_n^{k-1}, z^{k-1}] \right). \quad (30)$$

Then we compute the velocities \mathbf{u}_n^{k+1} and \mathbf{u}_s^{k+1} and the pressure p^{k+1} by solving the saddle point system

$$\mathcal{A} \begin{bmatrix} \mathbf{u}_n^{k+1} \\ \mathbf{u}_s^{k+1} \\ p^{k+1} \end{bmatrix} = \begin{bmatrix} \frac{1}{\Delta t} \mathcal{J}^{c \rightarrow f} \theta_n^k \mathbf{u}_n^k + \frac{\mu_n^v}{2} \Delta_h^{f \rightarrow f} [\theta_n^k] \mathbf{u}_n + D_h^{\text{stress}} \frac{\tau_n^{k+1} + \tau_n^k}{2} - \frac{\xi}{2} \mathcal{J}^{c \rightarrow f} \theta_n^k \theta_s^k (\mathbf{u}_n^k - \mathbf{u}_s^k) \\ \frac{1}{\Delta t} \mathcal{J}^{c \rightarrow f} \theta_s^k \mathbf{u}_s^k + \frac{\mu_s}{2} \Delta_h^{f \rightarrow f} [\theta_s^k] \mathbf{u}_s - \frac{\xi}{2} \mathcal{J}^{c \rightarrow f} \theta_n^k \theta_s^k (\mathbf{u}_s^k - \mathbf{u}_n^k) \\ 0 \end{bmatrix}, \quad (31)$$

in which \mathcal{A} is the linear operator defined by

$$\mathcal{A} = \begin{bmatrix} \mathcal{L} & \mathcal{G} \\ \mathcal{D} & 0 \end{bmatrix}, \quad (32)$$

in which

$$\mathcal{L} = \begin{bmatrix} \frac{1}{\Delta t} \mathcal{J}^{c \rightarrow f} \theta_n^{k+1} - \frac{\mu_n^v}{2} \Delta_h^{f \rightarrow f} [\theta_n^{k+1}] - \frac{\xi}{2} \mathcal{J}^{c \rightarrow f} \theta_n^{k+1} \theta_s^{k+1} & \frac{\xi}{2} \mathcal{J}^{c \rightarrow f} \theta_n^{k+1} \theta_s^{k+1} \\ \frac{\xi}{2} \mathcal{J}^{c \rightarrow f} \theta_n^{k+1} \theta_s^{k+1} & \frac{1}{\Delta t} \mathcal{J}^{c \rightarrow f} \theta_s^{k+1} - \frac{\mu_s}{2} \Delta_h^{f \rightarrow f} [\theta_s^{k+1}] - \frac{\xi}{2} \mathcal{J}^{c \rightarrow f} \theta_n^{k+1} \theta_s^{k+1} \end{bmatrix}, \quad (33)$$

$$\mathcal{G} = \begin{bmatrix} \mathcal{J}^{c \rightarrow f} \theta_n^{k+1} G_h^{c \rightarrow f} \\ \mathcal{J}^{c \rightarrow f} \theta_s^{k+1} G_h^{c \rightarrow f} \end{bmatrix}, \quad (34)$$

$$\mathcal{D} = \begin{bmatrix} -D_h^{f \rightarrow c} \mathcal{J}^{c \rightarrow f} \theta_n^{k+1} & -D_h^{f \rightarrow c} \mathcal{J}^{c \rightarrow f} \theta_s^{k+1} \end{bmatrix}. \quad (35)$$

The saddle point system in equation (31) is solved using GMRES. We precondition the system using a geometric multigrid method as described next.

3.4 Multigrid Preconditioner

We precondition the saddle point system in equation (31) with an FAC multigrid preconditioner [41] based on previous work by Wright et al. [33]. We construct additional coarser levels that cover the same physical space as Ω^0 . We denote these coarser levels by Ω^ℓ in which we now let ℓ be negative. These coarser patch levels are only used during the preconditioning step to smooth the solution. We define the prolongation operator $\mathcal{J}_{\ell \rightarrow \ell+1}$ as the operator that prolongs the solution from level Ω^ℓ to level $\Omega^{\ell+1}$. We also define the restriction operator $\mathcal{J}_{\ell \leftarrow \ell+1}$ as the operator that restricts the residual from level $\Omega^{\ell+1}$ to level Ω^ℓ . Both of these operators are constructed using a conservative linear interpolation procedure. We further denote explicitly the spatial dependence of solution operator \mathcal{A}_ℓ on a given patch level Ω^ℓ , in which \mathcal{A}_ℓ is a direct rediscrization of the multiphase equations. A single application of the preconditioner consists of one standard V-cycle [41].

During the pre- and post-smoothing steps, because of the presence of a zero block in the operator \mathcal{A}_ℓ in equation (32), standard relaxation schemes can not be applied directly. Therefore, we use the box relaxation smoother developed by Wright et al. [33]. For all the simulations shown, we use either three or five pre- and post-smoothing operations. On the coarsest level, which consists of either $N = 4, 8,$ or 16 grid points in each direction, we perform ten smoothing iterations. During each application of the smoother, we solve the following nine-by-nine system of equations in each grid cell

$$\begin{bmatrix} \mu_n^v \mathcal{L}^h[\theta_n] - \xi \mathcal{C}^h & \xi \mathcal{C}^h & \mathcal{G}^h[\theta_n] \\ \xi \mathcal{C}^h & \mu_s \mathcal{L}^h[\theta_s] - \xi \mathcal{C}^h & \mathcal{G}^h[\theta_s] \\ (\mathcal{G}^h[\theta_s])^T & (\mathcal{G}^h[\theta_s])^T & 0 \end{bmatrix} \begin{bmatrix} (\mathbf{u}_{ni,j})^{m+1} \\ (\mathbf{u}_{si,j})^{m+1} \\ (p_{i,j})^{m+1} \end{bmatrix} = \begin{bmatrix} F_n + \mu_n^v b[\theta_n, \mathbf{u}_n^{m+1}] \\ F_s + \mu_s b[\theta_s, \mathbf{u}_s^{m+1}] \\ 0 \end{bmatrix}, \quad (36)$$

in which components of \mathbf{u}_n and \mathbf{u}_s consist of velocity values stored at each grid cell face as follows

$$(\mathbf{u}_{ni,j})^{m+1} = \begin{bmatrix} (u_{i-1/2,j}^n)^{m+1} \\ (u_{i+1/2,j}^n)^{m+1} \\ (v_{i,j-1/2}^n)^{m+1} \\ (v_{i,j+1/2}^n)^{m+1} \end{bmatrix} \quad \text{and} \quad (\mathbf{u}_{si,j})^{k+1} = \begin{bmatrix} (u_{i-1/2,j}^s)^{m+1} \\ (u_{i+1/2,j}^s)^{m+1} \\ (v_{i,j-1/2}^s)^{m+1} \\ (v_{i,j+1/2}^s)^{m+1} \end{bmatrix},$$

and the operators $\mathcal{L}^h[\theta]$, \mathcal{C}^h , and $\mathcal{G}^h[\theta]$ are defined in the Appendix.

We process cells in a red-black ordering. We combine the smoother with under-relaxation to achieve better smoothing properties:

$$\begin{bmatrix} (\mathbf{u}_{ni,j})^{m+1} \\ (\mathbf{u}_{si,j})^{m+1} \\ (p_{i,j})^{m+1} \end{bmatrix} = (1 - \omega) \begin{bmatrix} (\mathbf{u}_{ni,j})^m \\ (\mathbf{u}_{si,j})^m \\ (p_{i,j})^m \end{bmatrix} + \omega \begin{bmatrix} \mu_n^v \mathcal{L}^h[\theta_n] - \xi \mathcal{C}^h & \xi \mathcal{C}^h & \mathcal{G}^h[\theta_n] \\ \xi \mathcal{C}^h & \mu_s \mathcal{L}^h[\theta_s] - \xi \mathcal{C}^h & \mathcal{G}^h[\theta_s] \\ (\mathcal{G}^h[\theta_s])^T & (\mathcal{G}^h[\theta_s])^T & 0 \end{bmatrix}^{-1} \begin{bmatrix} (F_n + \mu_n^v b[\theta_n, \mathbf{u}_n^{m+1}]) \\ (F_s + \mu_s b[\theta_s, \mathbf{u}_s^{m+1}]) \\ 0 \end{bmatrix}, \quad (37)$$

in which ω is the under-relaxation parameter. For all numerical experiments in the following section, we set $\omega = 0.75$. When applying the smoother on patch levels that do not cover the entire computational domain, we use the same ghost cell filling operation as described in Section 3.1 to fill ghost cells at coarse-fine interfaces. We note that in this case, the solution on the coarse grid is not changed by the application of the smoother.

3.5 Regridding Criteria

The locally refined meshes can be static, that is, they occupy a fixed region in the domain Ω^ℓ , or they can be adaptive, that is, certain cells undergo dynamic refinement based on a regridding criteria.

For a dynamic grid, after a specified number of time steps, we perform a regridding operation in which cells are tagged for refinement. In this work, cells are tagged for refinement based on the magnitude of the gradient of the volume fraction. Specifically, for each patch level ℓ , a cell $c_{i,j}^\ell$ is tagged for refinement if $\|\nabla_h \theta_{n_{i,j}}^\ell\| > \varepsilon^\ell$, in which

$$\nabla_h \theta_{n_{i,j}}^\ell = \left[\frac{\theta_{n_{i+1,j}}^\ell - \theta_{n_{i-1,j}}^\ell}{2\Delta x^\ell}, \frac{\theta_{n_{i,j+1}}^\ell - \theta_{n_{i,j-1}}^\ell}{2\Delta y^\ell} \right]^T, \quad (38)$$

is the discrete gradient of the network volume fraction, and ε^ℓ is the gradient tolerance threshold. Note that we are not restricted to using a particular criteria and more complex regridding criteria may be used for future applications. In newly refined regions, the velocities, $\mathbf{u}_n(\mathbf{x}, t)$ and $\mathbf{u}_s(\mathbf{x}, t)$, and pressure, $p(\mathbf{x}, t)$ are interpolated from the old coarse grid using a conservative linear interpolation scheme. In newly coarsened regions, all of the quantities are updated using conservative averages of the old fine grid data.

4 Results

We present convergence results for the numerical method for several test problems using manufactured solutions. The test problems include both prescribed volume fractions as well as evolved volume fractions for both uniform and statically refined grids. We also present results in an idealized four roll mill geometry for both a viscous and viscoelastic network. We show that the iteration count of the solver on the adaptive mesh is independent of grid spacing. We show that the numerical method offers significant speed and efficiency improvements for problems that require a high degree of resolution to capture interesting fluid flow phenomena, such as formation of singular structures in the network stress field, in dynamically-changing regions.

We define the L^1 , L^2 , and L^∞ discrete norms by

$$\|p\|_1 = \sum_{\ell=0}^{\ell_{\max}} \sum_{\text{valid}(i,j) \in \Omega^\ell} |p_{i,j}| \Delta x^\ell \Delta y^\ell, \quad (39)$$

$$\|p\|_2^2 = \sum_{\ell=0}^{\ell_{\max}} \sum_{\text{valid}(i,j) \in \Omega^\ell} p_{i,j}^2 \Delta x^\ell \Delta y^\ell, \quad (40)$$

$$\|p\|_\infty = \max_{\ell=0, \dots, \ell_{\max}} \max_{\text{valid}(i,j) \in \Omega^\ell} |p_{i,j}|, \quad (41)$$

in which a cell is valid if it is not covered by a refined cell. The solver is run on a sequence of grids with the coarsest grid having $N = 8$ points in each dimension up to $N = 128$ points. For cases in which we use a statically refined region, the refinement ratio is $r = 4$. The time step size, Δt , is chosen to satisfy the equation $\Delta t = C_{\text{CFL}} \Delta x / u_{\max}$ where the advective CFL number C_{CFL} is fixed to enforce solver stability. For all the simulations reported herein, we use periodic boundary conditions.

For simulations that use a statically refined region, we use an L-shaped region, as shown in Figure 6b. The re-entrant corner along the coarse-fine interface allows us to test the impact of this corner on overall accuracy. We note that the discretization utilized here does not conserve stresses along re-entrant corners, which may limit the effectiveness of the discretization at zero Reynolds numbers [42]. However, as we demonstrate herein, the discretization is effective at the non-zero Reynolds numbers tested.

Table 1: Parameter values for multiphase flow with (a) prescribed, variable volume fraction and (b) advecting volume fraction.

(a) Prescribed, variable volume fraction			(b) Advecting volume fraction		
Parameter	Symbol	Value	Parameter	Symbol	Value
Network viscosity	μ_n^v	4.0	Network Viscosity	μ_n^v	4.0
Solvent viscosity	μ_s	0.004	Solvent viscosity	μ_s	0.4
Drag coefficient	ξ	$250\mu_s$	Drag coefficient	ξ	$250\mu_s$
Density	ρ	1.0	Density	ρ	1.0
Maximum CFL number	C_{CFL}	0.5	Maximum CFL number	C_{CFL}	0.1

4.1 Multiphase flow with prescribed, variable volume fraction

This section analyzes the convergence behavior of the momentum solver when simulating multiphase flow with a prescribed, variable network volume fraction. The governing equations for this flow are given by equations (3) to (5). To analyze convergence of the solver, a manufactured test problem is set-up using forcing functions so that the solution components are given by

$$\mathbf{u}_n(\mathbf{x}, t) = \begin{pmatrix} \cos(2\pi(x-t)) \sin(2\pi(y-t)) \\ \sin(2\pi(x-t)) \cos(2\pi(y-t)) \end{pmatrix}, \quad (42a)$$

$$\mathbf{u}_s(\mathbf{x}, t) = \begin{pmatrix} -\cos(2\pi(x-t)) \sin(2\pi(y-t)) \\ -\sin(2\pi(x-t)) \cos(2\pi(y-t)) \end{pmatrix}, \quad (42b)$$

$$p(\mathbf{x}, t) = 0, \quad (42c)$$

$$\theta_n(\mathbf{x}, t) = \frac{1}{4} \sin(2\pi(x-t)) \sin(2\pi(y-t)) + \frac{1}{2}. \quad (42d)$$

We also use these functions as the initial conditions. The system parameters are defined in Table 1a.

The error norms between the numerical and analytical solution for the solution variables, $\mathbf{u}_n(\mathbf{x}, t)$, $\mathbf{u}_s(\mathbf{x}, t)$ and $p(\mathbf{x}, t)$, are calculated on both uniform grids and grids with locally refined, static L-shaped regions. The error norms vs. the grid size are plotted in Figures 2 and 3 for the simulations performed on uniform grids and static locally-refined grids, respectively. The plots show that the solver achieves second order accuracy for all solution variables across all error norms for the solutions obtained using a uniform grid and those obtained using a static locally-refined grid.

4.2 Multiphase flow with volume fraction advection

We allow the network and solvent volume fractions to advect with the fluid flow by solving an advection equation for $\theta_n(\mathbf{x}, t)$ and set $\theta_s(\mathbf{x}, t) = 1 - \theta_n(\mathbf{x}, t)$, in addition to solving the momentum equations. That is, we solve equations (1) and (3) to (5) to simulate multiphase Newtonian fluid flow for the case where the volume fractions $\theta_n(\mathbf{x}, t)$ and $\theta_s(\mathbf{x}, t)$ undergo advection with their respective velocity field. This means that $\theta_n(\mathbf{x}, t)$ is an additional solution component whose error norm with respect to grid size needs to be analyzed to determine the convergence behavior of the advection solver. To analyze convergence of the solver, a manufactured test problem is set-up using forcing functions so that the solution components are again given by equation (42).

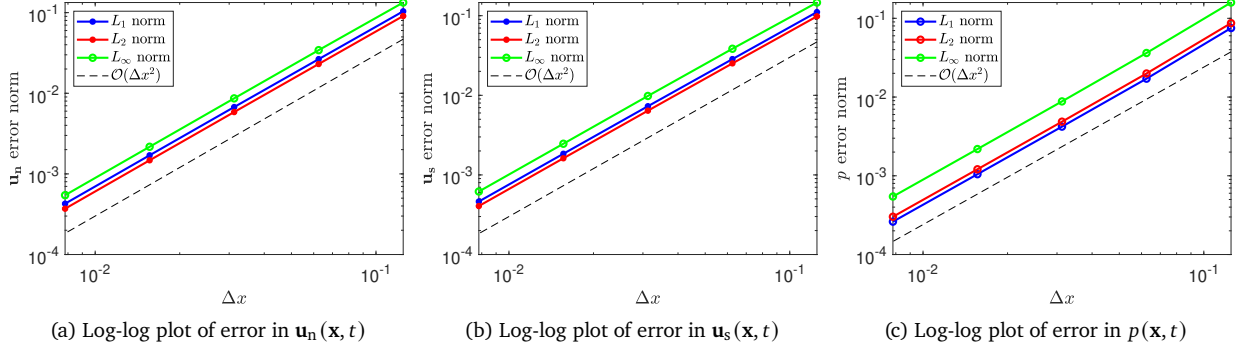


Figure 2: Log-log plots indicating convergence behavior of the momentum solver for a prescribed, variable network volume fraction $\theta_n(\mathbf{x}, t)$ on a uniform grid for each of the solution components: (a) $\mathbf{u}_n(\mathbf{x}, t)$, (b) $\mathbf{u}_s(\mathbf{x}, t)$, (c) $p(\mathbf{x}, t)$. We obtain second order convergence for all three solution components in the L^1 , L^2 and L^∞ norms.

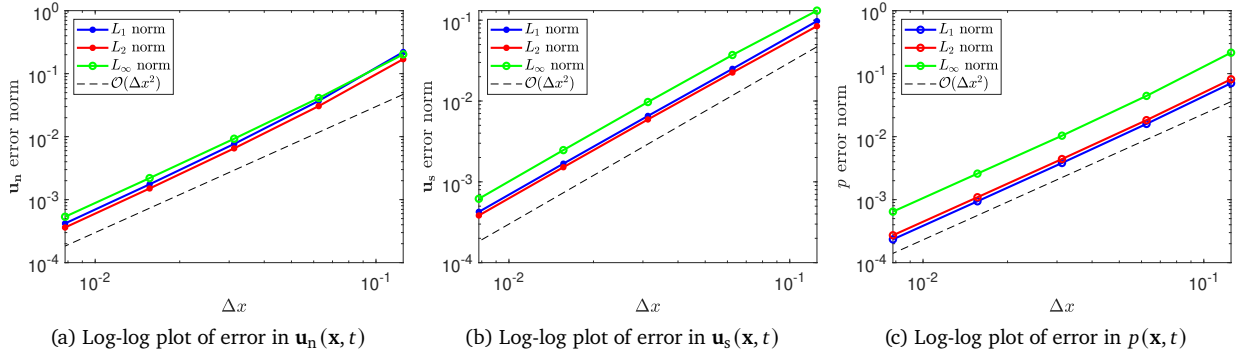


Figure 3: Log-log plots indicating convergence behavior of the momentum solver for a prescribed, variable network volume fraction $\theta_n(\mathbf{x}, t)$ on a static locally-refined grid for each of the solution components: (a) $\mathbf{u}_n(\mathbf{x}, t)$, (b) $\mathbf{u}_s(\mathbf{x}, t)$, (c) $p(\mathbf{x}, t)$. We obtain second order convergence for all three solution components in the L^1 , L^2 and L^∞ norms.

The remaining system parameters are defined in Table 1b. Because we are solving the full non-linear problem, additional time step size constraints must be followed, as shown by Wright et al. [33]. Here, we use a smaller maximum advective CFL number C_{CFL} to achieve a stable simulation.

As before, the error norms between the numerical and analytical solution for the solution variables, $\mathbf{u}_n(\mathbf{x}, t)$, $\mathbf{u}_s(\mathbf{x}, t)$, $p(\mathbf{x}, t)$, and $\theta_n(\mathbf{x}, t)$ are calculated on both uniform grids and grids with locally refined, static L-shaped regions. The error norms as a function of the grid size are plotted in Figures 4 and 5 for the simulations performed on uniform grids and static locally-refined grids, respectively. For the simulations performed using a uniform grid, the plots indicate that the solver achieves second order accuracy for all solution variables across all error norms. For the simulations performed using a static locally-refined L-shaped grid, the solver achieves between first and second order accuracy for all solution variables for each error norm. Note that this reduction in order of accuracy at coarse-fine interfaces is consistent with the first order discretization that is utilized at corners of the coarse-fine interface. This is illustrated in Figure 6a which shows the greatest error in the pressure at $t = 0.4$ is occurring near the re-entrant corner of the refined region and along the lengths of the coarse-fine interfaces adjacent to this corner.

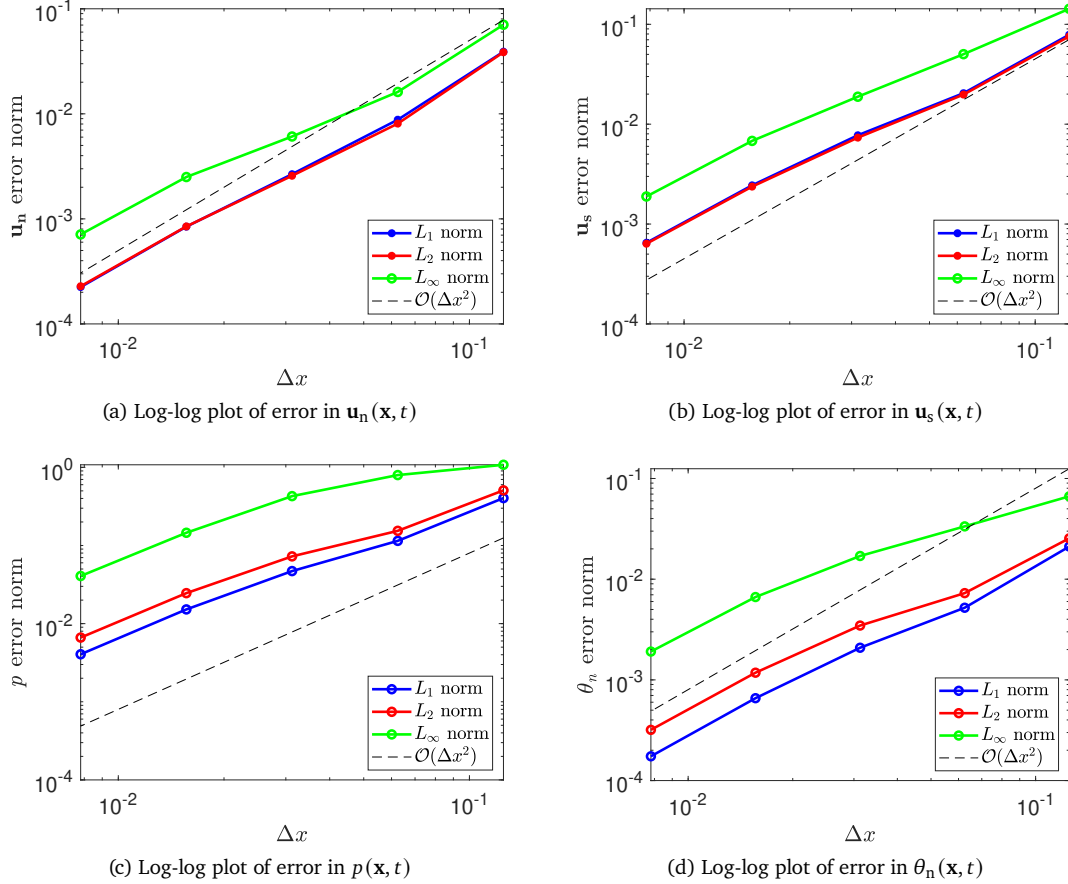


Figure 4: Log-log plots indicating convergence behavior of the fluid solver with advection of network volume fraction $\theta_n(\mathbf{x}, t)$ on a uniform grid for each of the solution components: (a) $\mathbf{u}_n(\mathbf{x}, t)$, (b) $\mathbf{u}_s(\mathbf{x}, t)$, (c) p and (d) $\theta_n(\mathbf{x}, t)$. We obtain second order convergence for all four solution components in the L^1 , L^2 and L^∞ norms.

4.3 Idealized Four Roll Mill

This experiment demonstrates the ability of the AMR solver to adaptively refine the mesh in critical regions of interest when simulating a two-phase flow model with a variable network volume fraction, $\theta_n(\mathbf{x}, t)$. We select the four roll mill first introduced by Taylor [43] as our test problem for illustrating the solver capabilities on an adaptive grid following the regridding criteria defined in Section 3.5. Here, the flow of the gel is driven by body forces, $\mathbf{f}_n(\mathbf{x}, t)$ and $\mathbf{f}_s(\mathbf{x}, t)$ acting on the network and solvent, respectively, resulting in the formation of vortices in each of the quadrants of the bi-periodic computational domain, $\Omega = [-0.5, 0.5] \times [-0.5, 0.5]$. The four roll mill has been used in other numerical studies of single-phase [17, 44] and two-phase viscous fluids [33]. The forces generate both rotational and extensional flow, with a stagnation point occurring at the center of the computational domain. For the viscoelastic fluid model, the extensional points generate large elastic stresses, which in single phase fluids with an Oldroyd-B model, can result in unbounded growth in the viscoelastic stress tensor for large enough Weissenberg numbers [17].

The initial network volume fraction is set to be a blob concentrated in a circular region of radius 0.175 centered at the origin as displayed in Figure 7. The exact form of the initial condition is

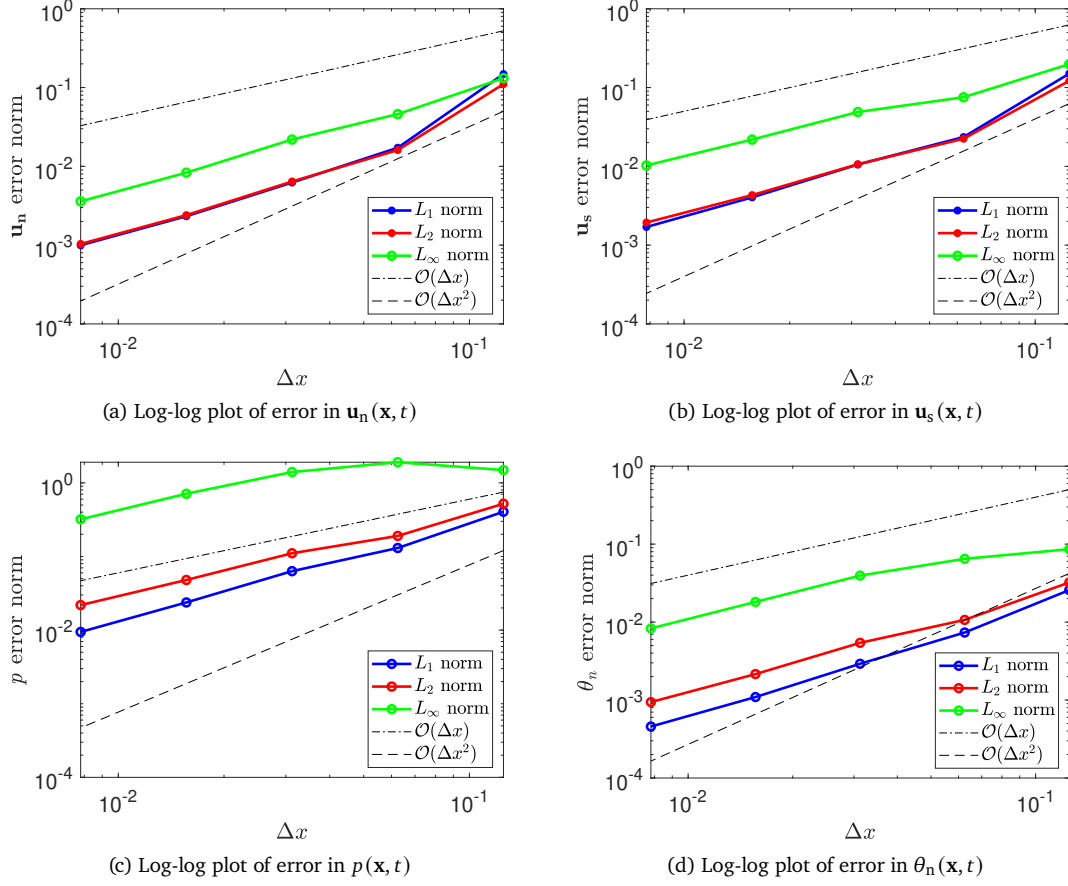


Figure 5: Log-log plots indicating convergence behavior of the fluid solver with advection of network volume fraction $\theta_n(\mathbf{x}, t)$ on a static locally-refined grid for each of the solution components: (a) $\mathbf{u}_n(\mathbf{x}, t)$, (b) $\mathbf{u}_s(\mathbf{x}, t)$, (c) $p(\mathbf{x}, t)$ and (d) $\theta_n(\mathbf{x}, t)$. The statically refined grid has an L-shaped refined region where the ratio of refinement between the coarse level and the refined level is $r = 2$. We obtain convergence that is asymptotically approaching second order accuracy for all four solution components in the L^1 , L^2 and L^∞ norms.

$$\theta_n(\mathbf{x}, 0) = \frac{1}{4} + \frac{1}{4} \begin{cases} \frac{1989}{896\pi} \left(1 - \left(\frac{x^2 + y^2}{\delta^2} \right)^4 \right)^4 \left(4 \left(\frac{x^2 + y^2}{\delta^2} \right)^4 + 1 \right)^4, & \text{if } x^2 + y^2 < \delta^2, \\ 0, & \text{otherwise,} \end{cases} \quad (43)$$

in which $\delta = 0.175$.

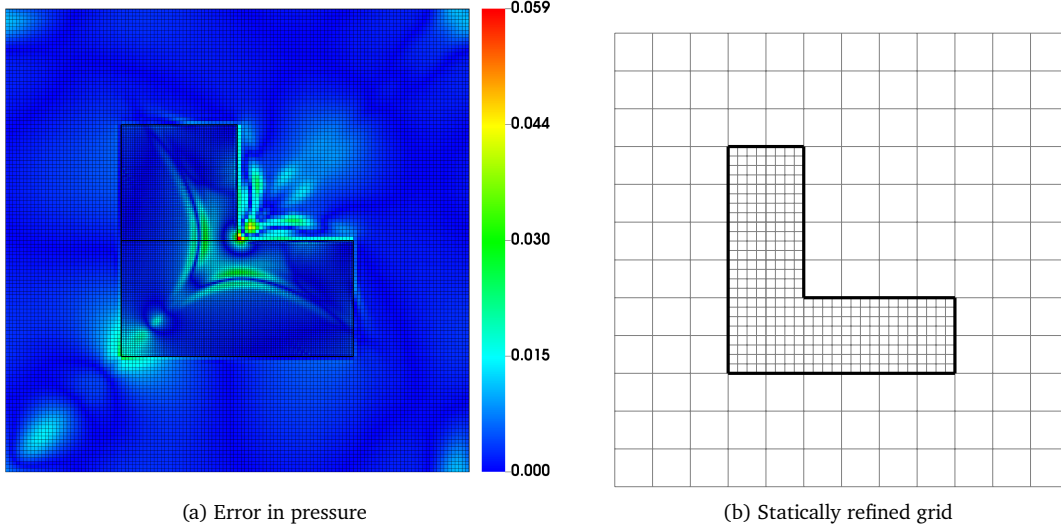


Figure 6: (a) The absolute error in pressure at $t = 0.4$ for the fluid simulation with advection of network volume fraction $\theta_n(\mathbf{x}, t)$ on a static locally-refined grid. The greatest error occurs near the re-entrant corner of the refined region and along the lengths of the coarse-fine interfaces adjacent to this corner. This is consistent with the first-order discretization implemented at corners of the coarse-fine interface. The statically refined grid in (b) has an L-shaped refined region where the ratio of refinement between the coarse level and the refined level is $r = 4$

The forcing functions $\mathbf{f}_n(\mathbf{x}, t)$ and $\mathbf{f}_s(\mathbf{x}, t)$ acting on the network and solvent, respectively, are defined as

$$\mathbf{f}_s(\mathbf{x}, t) = \mathbf{f}_n(\mathbf{x}, t) = \begin{bmatrix} (2\pi \sin(2\pi x) \cos(2\pi x) + 8\pi^2 \sin(2\pi x) \cos(2\pi y)) \\ (2\pi \sin(2\pi y) \cos(2\pi y) - 8\pi^2 \sin(2\pi y) \cos(2\pi x)) \end{bmatrix}. \quad (44)$$

We run two simulations, one with a Newtonian network and one with a viscoelastic network. The simulation parameters are given in Table 2. The shear viscosity values (μ_n^v, μ_s) are selected such that the network is 100 times more viscous than the solvent.

Table 2: Parameter values for the (a) Newtonian and (b) viscoelastic two-phase fluid simulations under four roll mill forcing.

(a) Newtonian Network			(b) Viscoelastic Network		
Parameter	Symbol	Value	Parameter	Symbol	Value
Network Viscosity	μ_n^v	4.0	Network viscosity	μ_n^v	2.0
Solvent viscosity	μ_s	0.04	Solvent viscosity	μ_s	0.04
Polymer relaxation time	λ	0.3	Polymeric contribution to viscosity	μ_n^p	2.0
Drag coefficient	ξ	$250 \mu_s$	Polymer relaxation time	λ	4.0
Density	ρ	1.0	Drag coefficient	ξ	$250 \mu_s$
Maximum CFL number	CFL	0.1	Density	ρ	1.0

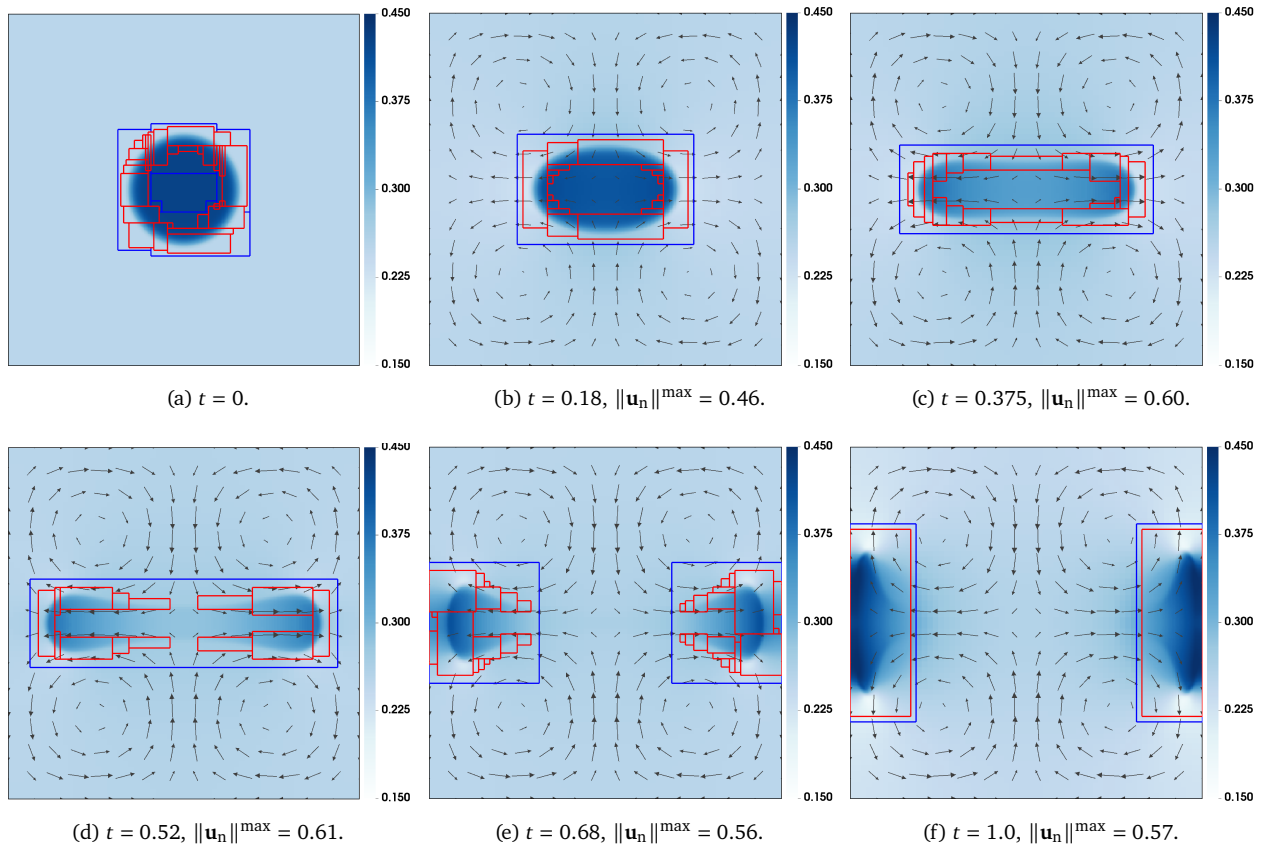


Figure 7: Simulation results for a blob of viscous network immersed in a viscous solvent bath, with the mixture driven by four roll mill forcing. The distribution of $\theta_n(\mathbf{x}, t)$ and $\mathbf{u}_n(\mathbf{x}, t)$ at various times on an AMR grid are plotted, whereby the coarsest level grid size is 64×64 . The grid is adaptively refined with up to 2 additional levels of refinement, as indicated by the blue and red levels, if the absolute gradient of $\theta_n(\mathbf{x}, t)$ exceeds 0.75 for both Ω^0 and Ω^1 . Vectors at different times have the same scale.

4.3.1 Convergence of Newtonian Network

We simulate a two-phase viscous mixture consisting of a Newtonian network immersed in a solvent bath subject to four roll mill forcing with fluid parameters as outlined in Table 2a. The simulation employs an AMR grid and runs up to a final time of $T = 1.0$. The plots of the distribution of $\theta_n(\mathbf{x}, t)$ and $\mathbf{u}_n(\mathbf{x}, t)$ at different times are shown in Figure 7. The coarsest level, Ω^0 , of the AMR grid is of size 64-by-64 and covers the entire computational domain. The solver uses two additional levels of refinement, Ω^1 and Ω^2 , with coarse-to-fine refinement ratios of two between each level. These refined levels appear in the plot with blue and red outlines, respectively. The plots indicate that the fluid solver is able to adaptively refine regions of interest, which in this case are areas where the absolute gradient of $\theta_n(\mathbf{x}, t)$ exceeds a threshold of 0.75 for both levels, Ω^0 and Ω^1 . Initially, the refined levels cover the entire blob of network immersed in the solvent bath. As time goes on, the four roll mill forcing results in extension of the blob of network. As the blob extends horizontally, the network volume fraction accumulates at the ends of the elongated blob. The refined regions follow the edge of the blob, as it fully separates into two blobs.

Since we do not know the analytical solution to two-phase viscous flow under four roll mill forcing, we approx-

Table 3: Order of accuracy, k , at $t = 0.15$ using three solutions with coarsest level grid sizes (a) $N = 16$, $N = 32$, $N = 64$, and (b) $N = 32$, $N = 64$, $N = 128$, corresponding to solutions f_{4h} , f_{2h} , f_h , respectively. The solver is asymptotically approaching second order convergence in the L^1 , L^2 and L^∞ norm as the grids are refined.

Component	Order of accuracy, k					
	L^1 norm		L^2 norm		L^∞ norm	
	(a)	(b)	(a)	(b)	(a)	(b)
$\mathbf{u}_n(\mathbf{x}, t)$	1.713	1.796	1.738	1.912	1.162	1.943
$\mathbf{u}_s(\mathbf{x}, t)$	1.773	2.220	1.784	2.293	1.384	2.012
$\theta_n(\mathbf{x}, t)$	0.967	1.652	1.375	1.966	1.128	2.000
$p(\mathbf{x}, t)$	1.489	1.601	1.032	1.643	0.770	1.457

Table 4: Order of accuracy, k , at $t = 0.18$ using three solutions with coarsest level grid sizes (a) $N = 16$, $N = 32$, $N = 64$, and (b) $N = 32$, $N = 64$, $N = 128$, corresponding to solutions f_{4h} , f_{2h} , f_h , respectively. The solver is asymptotically approaching second order convergence in the L^1 , L^2 and L^∞ norm as the grids are refined.

Component	Order of accuracy, k					
	L^1 norm		L^2 norm		L^∞ norm	
	(a)	(b)	(a)	(b)	(a)	(b)
$\mathbf{u}_n(\mathbf{x}, t)$	2.054	1.714	2.117	1.791	2.683	1.024
$\mathbf{u}_s(\mathbf{x}, t)$	2.201	2.131	2.244	2.144	1.955	1.621
$\theta_n(\mathbf{x}, t)$	0.983	1.620	1.184	1.931	0.680	2.015
$p(\mathbf{x}, t)$	1.232	1.680	0.857	1.685	0.254	1.682

imate the order of convergence k using Richardson extrapolation:

$$k = \log_2 \left(\frac{\|f_{4h} - f_{2h}\|_p}{\|f_{2h} - f_h\|_p} \right), \quad (45)$$

in which f_{4h} , f_{2h} , f_h are the solutions on grids where the size of the coarsest level is increased, but the number of patch levels and the refinement ratios are held fixed.

Since we are dealing with adaptively refined grids, f_h is the solution obtained on a computational domain whose coarsest level has a grid spacing of h . The norm of difference, $\|f_h - f_{2h}\|_p$ is calculated by interpolating the fine solution, f_h , onto the coarser AMR patch hierarchy, f_{2h} whose coarsest level has a grid spacing of $2h$.

The order of accuracy values at $t = 0.15$ and $t = 0.18$ are presented in Tables 3 and 4. These times are selected for computing convergence behavior because these are times before the blob begins to separate. Beyond these times, pressures with sharp gradients form as the blob fully separates, as shown in Figure 8, and these limit the convergence of the method. We expect that with sufficient resolution, second order accuracy will be restored. The data in these tables shows that the solver achieves convergence for all components across all norms, whereby the solver is asymptotically approaching second order convergence in the L^1 , L^2 and L^∞ norm as the grids are refined.

To illustrate that the number of iterations required for the linear solver to converge at each time step is independent of grid spacing, we plot the number of iterations it takes for the linear solver to achieve a relative residual

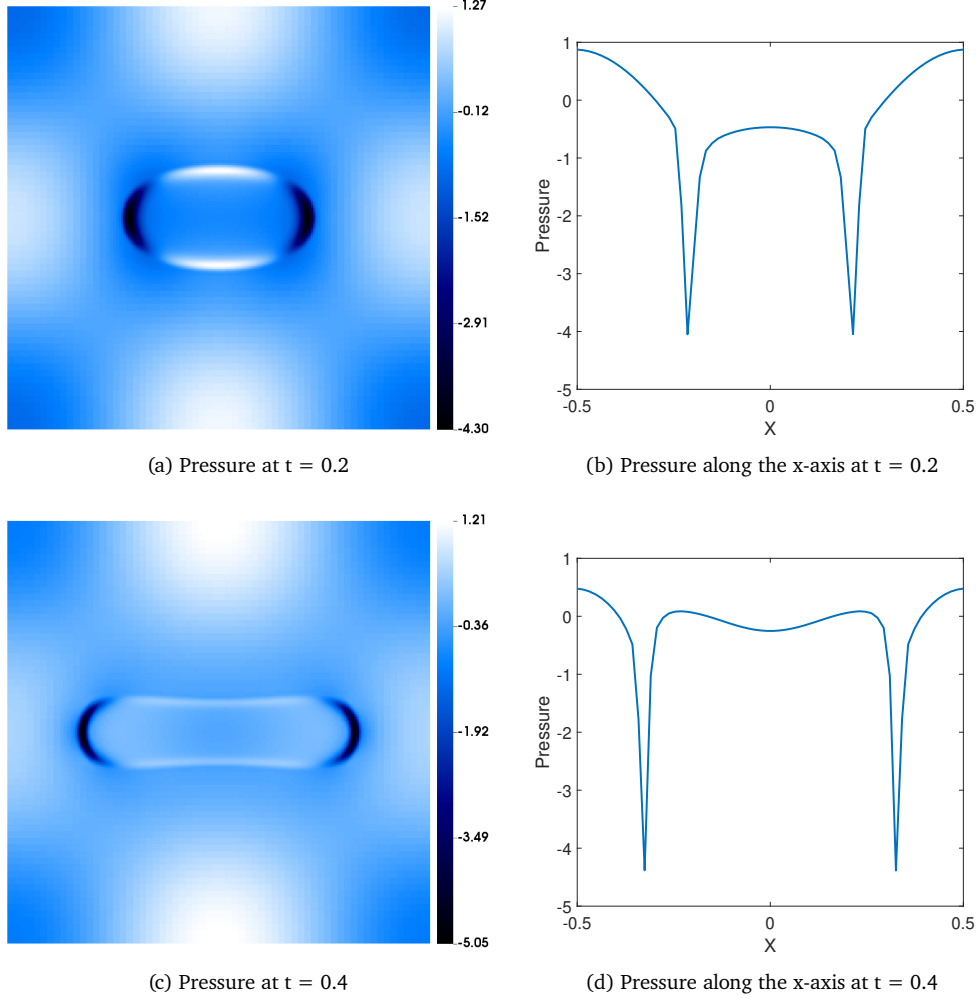


Figure 8: The (a,c) pressure distribution over the whole domain and (b,d) pressure distribution along the x-axis at two different times for the Newtonian network under four roll mill forcing simulated on an AMR grid. The sharp pressure gradients can be observed in the 1D pressure distribution plots in (b,d).

tolerance of 10^{-14} against the time step number. We calculate a rolling average by computing the mean number of iterations needed to converge every 640 time steps. Figure 9 shows that the linear solver remains relatively consistent throughout the simulation time for a given AMR grid, and the number of iterations taken to achieve convergence at each time step is very similar across the different grids, with the value always falling between 19 to 23 iterations. This indicates that the multigrid solver serves as an effective preconditioner on adaptive grids.

4.3.2 Convergence of Viscoelastic Network

We simulate a two-phase viscoelastic fluid that is subject to four roll mill forcing using a uniform grid to showcase the convergence behavior of our solver. The advected quantities, $\theta_n(\mathbf{x}, t)$ and $z(\mathbf{x}, t)$, are initially set to spatially-uniform values of 0.5 and 1.0, respectively, and are advected with the network velocity field. The stress tensor, $\sigma_{ve}(\mathbf{x}, t)$, is initially set to the identity tensor. The fluid parameters are outlined in Table 5. This set-up was

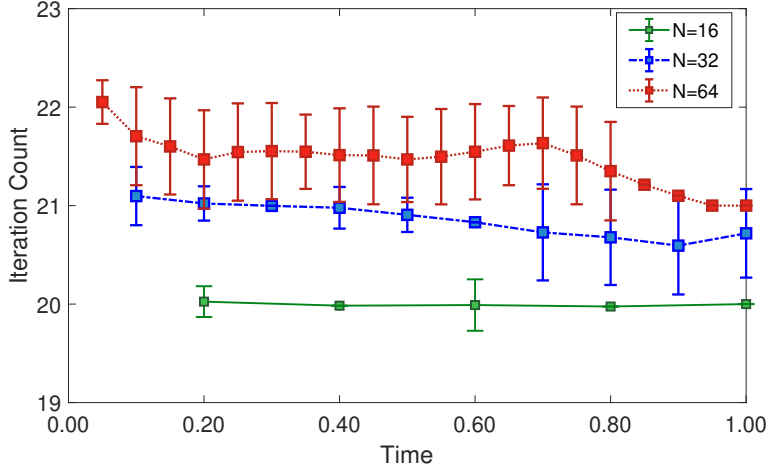


Figure 9: A rolling average (computed every $640\Delta t$) of the number of iterations against the time to converge to a relative residual tolerance of 10^{-14} for the blob of viscous network immersed in a viscous solvent bath under four roll mill forcing simulated using different AMR grid sizes. N refers to the size of the coarsest level grid on the patch hierarchy. Since the iteration count is confined to a narrow range of 19 to 23, there is clear evidence that the number of iterations required for the solver to converge at each time step is independent of the grid spacing.

selected because, while it is a relatively simple set of initial conditions, the simulation produces non-trivial results as shown in Figure 10. The order of accuracy k at two different times is obtained using Richardson’s extrapolation as in equation (45). Convergence results are presented in Tables 6 and 7 and the corresponding distributions of the trace of the stress tensor and the network volume fraction are displayed in Figure 10.

Table 5: Parameter values for the two-phase viscoelastic fluid under four roll mill forcing on a uniform grid.

Parameter	Symbol	Value
Network Viscosity	μ_n^v	2.0
Solvent Viscosity	μ_s	0.04
Polymeric contribution to Viscosity	μ_n^p	2.0
Polymer Relaxation Time	λ	2.0
Drag Coefficient	ξ	$250 \mu_s$
Density	ρ	1.0

From these convergence studies, we see that the solver obtains second order accuracy for velocities, volume fraction, pressure, and components of the stress tensor in the L^1 and L^2 norms. We attain at least 1st order accuracy in the L^∞ norm, with most variables approaching second order of accuracy in the L^∞ norm as well. In particular, the off-diagonal component, $\sigma_{xy}(\mathbf{x}, t)$, of the stress tensor only achieves an order of accuracy of 1.5 in the L^∞ at the final time. Note that the advection scheme utilized here reduces to a first order approximation near regions of large gradients or discontinuities, limiting pointwise accuracy to first order.

Plots of the distribution of the trace of the stress tensor, $\text{tr}(\sigma_{ve}(\mathbf{x}, t))$, along with the network volume fraction,

Table 6: Order of accuracy, k , at $t = 0.5$ using three solutions with coarsest level grid sizes: $N = 64$, $N = 128$, $N = 256$, corresponding to solutions f_{4h} , f_{2h} , f_h , respectively. The solver obtains second order accuracy in the L^1 and L^2 norms and attains at least 1st order accuracy in the L^∞ norm, with most variables approaching second order accuracy in the L^∞ norm.

Component	Order of accuracy, k		
	L^1 norm	L^2 norm	L^∞ norm
$\mathbf{u}_n(\mathbf{x}, t)$	2.166	2.502	2.401
$\mathbf{u}_s(\mathbf{x}, t)$	2.069	2.112	2.450
$\theta_n(\mathbf{x}, t)$	2.325	2.257	1.627
$p(\mathbf{x}, t)$	2.237	2.262	1.716
$\sigma_{xx}(\mathbf{x}, t)$	2.374	2.176	1.615
$\sigma_{yy}(\mathbf{x}, t)$	2.374	2.176	1.615
$\sigma_{xy}(\mathbf{x}, t)$	1.996	1.755	1.325

Table 7: Order of accuracy, k , at $t = 1.0$ using three solutions with coarsest level grid sizes: $N = 64$, $N = 128$, $N = 256$, corresponding to solutions f_{4h} , f_{2h} , f_h , respectively. The solver obtains second order accuracy in the L^1 and L^2 norms and attains at least 1st order accuracy in the L^∞ norm, with most variables approaching second order accuracy in the L^∞ norm.

Component	Order of accuracy, k		
	L^1 norm	L^2 norm	L^∞ norm
$\mathbf{u}_n(\mathbf{x}, t)$	2.253	1.980	1.709
$\mathbf{u}_s(\mathbf{x}, t)$	1.876	1.917	1.809
$\theta_n(\mathbf{x}, t)$	1.982	1.861	1.605
$p(\mathbf{x}, t)$	1.841	1.822	1.800
$\sigma_{xx}(\mathbf{x}, t)$	2.178	2.161	1.810
$\sigma_{yy}(\mathbf{x}, t)$	2.178	2.161	1.811
$\sigma_{xy}(\mathbf{x}, t)$	2.030	1.838	1.537

$\theta_n(\mathbf{x}, t)$, are shown in Figure 10. The background forcing due to the four roll mill is apparent by the symmetrical distribution of $\theta_n(\mathbf{x}, t)$. The lowest $\theta_n(\mathbf{x}, t)$ occurs in regions where the magnitude of $\mathbf{u}_n(\mathbf{x}, t)$ is greatest since it is being advected away by the high network velocity, and the greatest $\theta_n(\mathbf{x}, t)$ accumulates in regions where the magnitude of $\mathbf{u}_n(\mathbf{x}, t)$ is the lowest. We observe formation of cusps in $\text{tr}(\sigma_{ve}(\mathbf{x}, t))$ as the simulation proceeds, and the value of $\text{tr}(\sigma_{ve}(\mathbf{x}, t))$ is greatest at locations with stagnation points. These also happen to be locations where $\theta_n(\mathbf{x}, t)$ is observed to accumulate the most by virtue of being advected towards these stagnation points by the background four roll mill forcing.

4.3.3 Relaxation of Viscoelastic Network

We demonstrate the robustness and efficiency of our computational AMR solver by simulating the dynamics of a viscoelastic material. Simulations such as the one presented in this section are beneficial in the study of soft matter, such as gels, elastomers and biological tissue, which have numerous applications in nature and

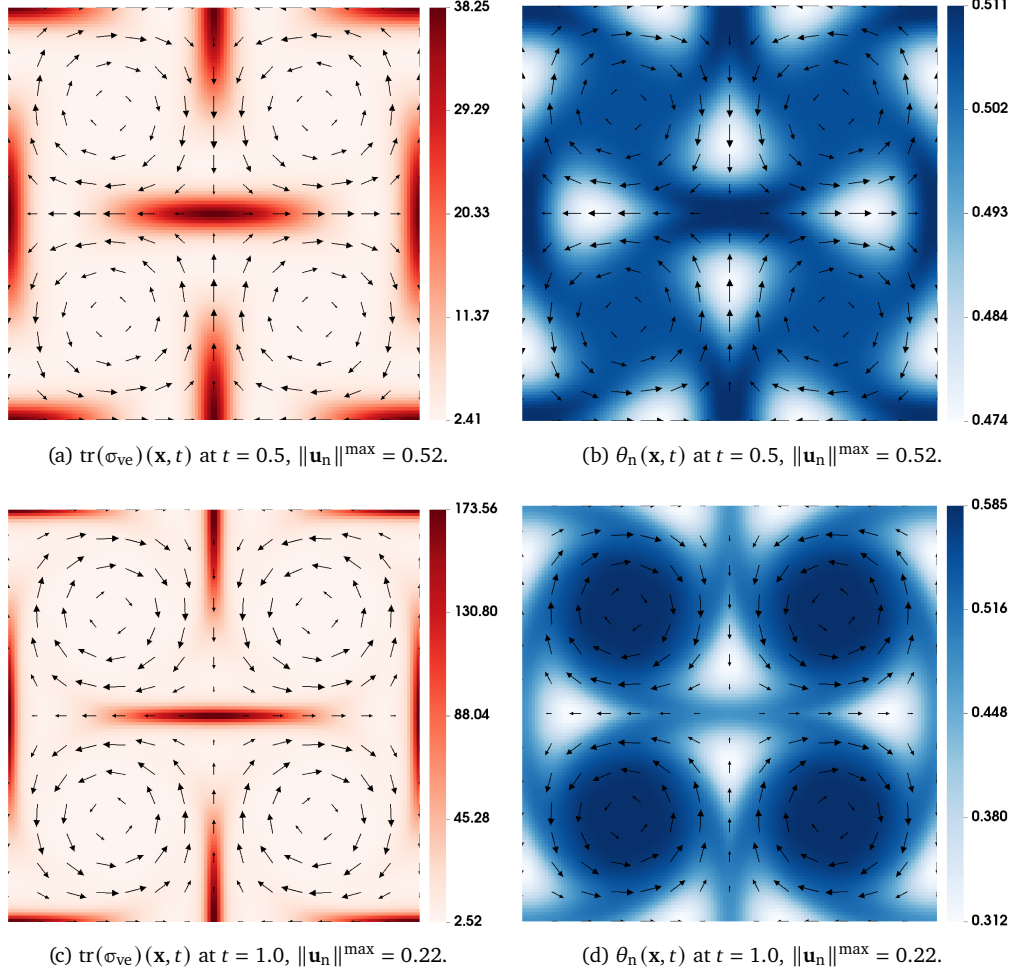


Figure 10: The distribution of (a,c) the trace of $\sigma_{ve}(\mathbf{x}, t)$ and (b,d) $\theta_n(\mathbf{x}, t)$ at $t = 0.5$ and $t = 1.0$ along with the network velocity field, $\mathbf{u}_n(\mathbf{x}, t)$, on a uniform grid of size 128×128 . Initially, $\theta_n(\mathbf{x}, t)$ is distributed uniformly across the entire domain and gets advected due to four roll mill forcing, resulting in the distribution shown in (b,d). The background forcing causes the multiphase fluid to elongate along the x-axis and compress along the y-axis. This is apparent from the distribution of $\text{tr}(\sigma_{ve})(\mathbf{x}, t)$, which develops cusps (identified by taking a cross-section across the dark shaded regions to reveal a symmetric curve with a singularity point) as the simulation proceeds, and achieves the greatest values at locations with stagnation points. Vectors at different times do not have the same scale.

engineering due to their high versatility. To that end, we simulate a multiphase viscoelastic fluid model based on those used in clotting models [5, 35]. We subject this fluid model to four roll mill forcing and simulate its behaviour using an AMR grid up to time $T = 2.0$, with fluid parameters as outlined in Table 2b. The parameters are selected to match the fluid parameters of the four roll mill simulation presented in Section 4.3.1. In particular, the network viscosity is split equally into a viscous contribution and a polymeric contribution whose sum is equal to the viscosity of the Newtonian network simulated previously. The AMR grid used in the simulation has a total of four refinement levels, Ω^0 to Ω^3 , starting with a 32-by-32 grid on the coarsest level which covers the entire

computational domain $\Omega = [-0.5, 0.5] \times [-0.5, 0.5]$. The refinement ratios are 4, 2, and 2, starting from the coarsest level to the finest level. The initial network volume fraction is set to be concentrated in a circular region of radius 0.175 centered at the origin, as defined in equation (43). The forcing functions acting on the network and solvent are

$$\mathbf{f}_s(\mathbf{x}, t) = \mathbf{f}_n(\mathbf{x}, t) = \begin{cases} \begin{bmatrix} (2\pi \sin(2\pi x) \cos(2\pi x) + 8\pi^2 \sin(2\pi x) \cos(2\pi y)) \\ (2\pi \sin(2\pi y) \cos(2\pi y) - 8\pi^2 \sin(2\pi y) \cos(2\pi x)) \end{bmatrix}, & \text{if } t < 0.20, \\ \mathbf{0}, & \text{otherwise,} \end{cases} \quad (46)$$

The background forces are conditionally set to act on the phases if $t < 0.20$, after which they are switched off. We define the Weissenberg number as $Wi = \frac{\lambda}{\tau_f}$, in which τ_f is the characteristic time scale of the fluid. The Weissenberg number measures the relaxation of the fluid to the transient processes in the fluid. For large Weissenberg numbers $Wi \gg 1.0$, the fluid maintains substantial elastic energies and generates large elastic forces over time. As done by Thomases and Shelley [17], we choose the time scale of the fluid to be set by the dimensional scaling of the force $\tau_f = \frac{\mu_n^v + \mu_n^p}{LF}$ in which $F = 8\pi^2$ and $L = 1$ is the length of the computational domain. This gives a Weissenberg number of approximately $Wi \approx 80$.

The distribution of the network volume fraction $\theta_n(\mathbf{x}, t)$ along with the network velocity field $\mathbf{u}_n(\mathbf{x}, t)$ is plotted in Figure 11 at several different times. From $t = 0$ to $t = 0.20$, the network blob experiences forces that tend to pull it apart horizontally, as well as forces that cause compression in the vertical direction. When the background forcing is turned off at $t = 0.20$, the network blob continues to stretch horizontally because of the presence of inertia in the system. At around $t = 0.4$, the stretching subsides and the blob begins returning to its initial state because of the elasticity of the fluid. The flow dynamics are now dominated by the relaxation of the elastic stresses and the network velocity reverses direction. As the blob of network shrinks, the solvent (not pictured) is correspondingly pushed away from the center of the blob. Each level in the patch hierarchy, from Ω^0 to Ω^3 , adaptively refines itself by the prescribed refinement ratio, r , whenever the absolute gradient of the network volume fraction exceeds 0.2, 0.8 and 1.75, respectively. The mesh is able to maintain a high resolution near the edge of the blob where the network volume fraction has a steep gradient, while retaining a coarse grid in areas away from the network blob, as indicated by the refinement levels in Figure 11.

The number of iterations needed to achieve convergence at each time step were computed and the results are plotted in Figure 12. We use a relative residual tolerance of 10^{-8} as our convergence criteria and compute a rolling average of the number of iterations needed to converge. The iteration count remains confined between 19 and 20, which indicates that the solver is robust and efficient for simulating a complex fluid model with adaptive mesh refinement. The moving average increases slightly after $t = 0.6$ which is consistent with when the blob of network begins to shrink towards its initial state and the network velocity field reverses direction.

4.4 Comparing Computational Cost between AMR and Uniform Grids

To demonstrate the significant savings in computational costs, we perform timing experiments using the solver on both uniform and adaptively refined grids. We perform four roll mill simulations for both the Newtonian network and the viscoelastic network from $t = 0$ to $t = 1$ on different grids whereby the size, N , of the coarsest level is increased, but the number of patch levels and refinement ratios are held fixed for each simulation. We use a total of 3 adaptive refinement levels, Ω^0 to Ω^2 , for the AMR simulations for both network types. For the Newtonian network on the AMR grid, a refinement ratio of $r^{(1)} = r^{(2)} = 2$ is used between consecutive levels.

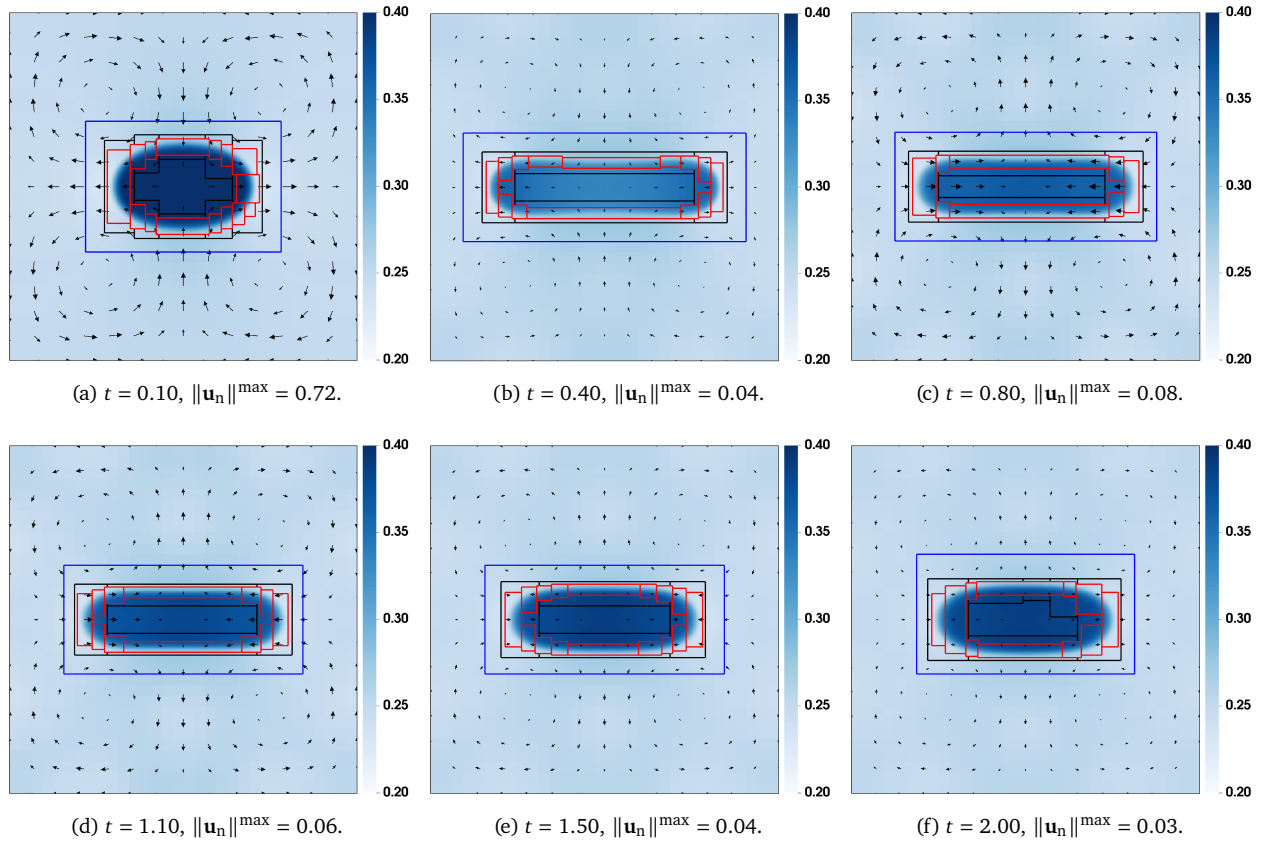


Figure 11: Simulation results for a blob of viscoelastic network immersed in a viscous solvent bath, subject to four roll mill forcing. The distribution of $\theta_n(\mathbf{x}, t)$ and the network velocity, $\mathbf{u}_n(\mathbf{x}, t)$, are plotted at various times on an AMR grid with a coarsest level of size 32×32 and 3 additional nested levels of refinement, as indicated by the blue, black and red lines, with refinement ratios of 4, 2, and 2, respectively, between levels. Vectors at different times do not have the same scale.

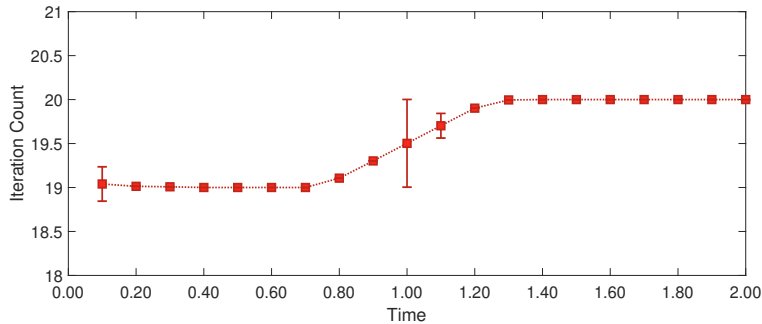


Figure 12: A plot of the rolling average (computed every $500\Delta t$) of the number of iterations as a function of time needed to converge to a relative residual tolerance of 10^{-8} for the blob of viscoelastic network immersed in a viscous solvent bath under four roll mill forcing simulated using an AMR grid. Since the iteration count is confined to a narrow range of 19 to 20, there is clear evidence that solver convergence is consistent across the whole simulation regardless of the shape and size of the AMR grid.

For the viscoelastic network on the AMR grid, refinement ratios of $r^{(1)} = 2$ and $r^{(2)} = 4$ are used between levels in the AMR hierarchy. We note that this setup is different from that used in Section 4.3.3 because of the prohibitive expense of running the corresponding uniform grid simulation. Figure 13 shows the time taken using an AMR grid as a percentage of the time taken using a uniform grid to generate four roll mill simulations with (a) a Newtonian network and (b) a viscoelastic network. The size of the uniform grid covering the computational domain is determined using the size of the finest level of the AMR grid. The results indicate that AMR offers a major cost savings benefit, providing up to 10x speed-up in the numerical experiments presented here, with greater speedup observed as the finest spatial resolution is increased. The speed-up is not limited to the results presented here and increased speed-up can be achieved depending on the problem setup.

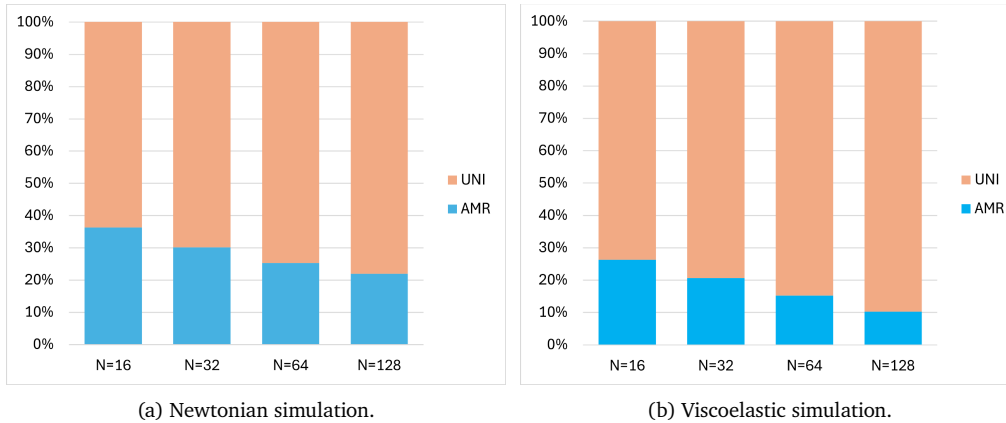


Figure 13: Plots showing the time taken to complete four roll mill simulations using an AMR grid as a percentage of the time taken using a uniform grid with (a) a Newtonian network and (b) a viscoelastic network. The AMR grid in both (a) and (b) uses a total of 3 adaptive refinement levels. For the Newtonian network on the AMR grid, a refinement ratio of $r^1 = r^2 = 2$ is used between consecutive levels. For the viscoelastic network on the AMR grid, refinement ratios of $r^1 = 2$ and $r^2 = 4$ are used between levels in the AMR hierarchy. The value of N indicates the size of the coarsest level of the AMR grid. The size of the uniform grid is determined using the size of the finest level of the AMR grid. It is observed that AMR offers major cost savings, yielding up to 10x speedup in our experiments, whereby greater speedup is observed as the finest spatial resolution is increased.

5 Conclusion

Multiphase flows are encountered in a range of diverse settings, ranging from natural phenomena to biomedical applications. In order to study multiphase systems, a widely-used approach is to describe each phase as a continuum in which each point in space can be occupied by a mixture of phases, while additionally specifying the velocity field and stresses of each phase. Depending on the choice of constitutive equation for the Cauchy stress, each phase can be modeled as either a Newtonian or non-Newtonian (complex) fluid. The resulting coupled system of equations pose numerical challenges due to the presence of multiple non-linear terms and a co-incompressibility condition, while the resulting fluid dynamics arising from the model necessitate the development of an adaptive mesh refinement technique to accurately capture regions of interest while keeping computational costs low.

We have presented an accurate, robust, and efficient computational method for simulating multiphase mixtures

on adaptive grids. We use second order accurate finite differences to discretize the differential operators, and the resulting saddle point system is solved using a Krylov method with preconditioning. We adapt a robust geometric multigrid preconditioner with box relaxation smoothing to solve the system on an adaptively refined grid. For single-phase fluids, projection-based methods are simple and effective for solving the momentum equations. However, the co-incompressibility condition leads to additional complications making the details of a projection method unclear. As our numerical studies indicate that the geometric multigrid preconditioner is expensive, future studies will focus on developing efficient projection or block factorization preconditioners, which have yet to be developed for this system. To advance the solution in time, we discretize the viscous stress and drag using an implicit trapezoidal rule and discretize the transport equations using a second order Adams-Bashforth scheme.

We presented convergence behavior on uniform and refined grids for both prescribed volume fractions and evolved volume fractions. Our results indicate that the solver achieves second order accuracy in the L^1 and L^2 norms and approaches second order accuracy in the L^∞ norm. We generated four-roll mill simulations for a Newtonian fluid model and a viscoelastic fluid model that has both viscous and viscoelastic stresses. We demonstrated that the AMR solver on the Newtonian model asymptotically approaches second order convergence in the L^1 , L^2 and L^∞ norms for all solution variables. For the viscoelastic model subject to four roll mill forcing on a uniform grid, we showed that the solver obtains second order accuracy for solution components in the L^1 and L^2 norms and attains at least 1st order accuracy in the L^∞ norm. The final experiment presented a simulation of the viscoelastic fluid model that undergoes deformation up to a certain time after which the forces are turned off, allowing the viscoelastic polymer network to relax to a state of equilibrium. An AMR grid with multiple nested refinement levels was employed for this simulation and we observed that it can sufficiently resolve sharp gradients in the volume fractions. All experiments demonstrated the solver is stable provided the time step size satisfies the imposed CFL condition. An investigation into the iteration count at every time step showed that the multigrid solver is robust because its performance remains independent of grid spacing.

Acknowledgments

We gratefully acknowledge funding from NIH grants 1R01GM131408, U01HL143336, and R01HL157631 as well as NSF OAC 1931516.

References

- [1] C. G. Philippesen, A. C. F. Vilela, and L. D. Zen. “Fluidized Bed Modeling Applied to the Analysis of Processes: Review and State of the Art”. In: *Journal of Materials Research and Technology* 4.2 (2015), pp. 208–216.
- [2] H. Zhang, X. Tan, and X. Zheng. “Multifield Intermittency of Dust Storm Turbulence in the Atmospheric Surface Layer”. In: *Journal of Fluid Mechanics* 963 (2023), A15.
- [3] M. Ouda and E. A. Toorman. “Development of a New Multiphase Sediment Transport Model for Free Surface Flows”. In: *International Journal of Multiphase Flow* 117 (2019), pp. 81–102.
- [4] A. F. Moench. “Double-Porosity Models for a Fissured Groundwater Reservoir With Fracture Skin”. In: *Water Resources Research* 20.7 (1984), pp. 831–846.

- [5] J. Du and A. L. Fogelson. “A Two-phase Mixture Model of Platelet Aggregation”. In: *Mathematical Medicine and Biology* 35.2 (2018), pp. 225–256.
- [6] M. R. K. Mofrad and R. D. Kamm, eds. *Cytoskeletal Mechanics: Models and Measurements*. Cambridge ; New York: Cambridge University Press, 2006.
- [7] C. Tongu, T. Kenmotsu, Y. Yoshikawa, A. Zinchenko, N. Chen, and K. Yoshikawa. “Divalent Cation Shrinks DNA but Inhibits Its Compaction with Trivalent Cation”. In: *The Journal of Chemical Physics* 144.20 (2016), p. 205101.
- [8] J. Du, B. M. Nagda, O. L. Lewis, D. B. Szyld, and A. L. Fogelson. “A Computational Framework for the Swelling Dynamics of Mucin-like Polyelectrolyte Gels”. In: *Journal of Non-Newtonian Fluid Mechanics* 313 (2023), p. 104989.
- [9] B. M. Nagda, J. Du, O. L. Lewis, and A. L. Fogelson. “Deswelling Dynamics of Chemically-Active Polyelectrolyte Gels”. In: *Computational Science – ICCS 2023*. Ed. by J. Mikyška, C. De Mulatier, M. Paszynski, V. V. Krzhizhanovskaya, J. J. Dongarra, and P. M. Slood. Vol. 14077. Cham: Springer Nature Switzerland, 2023, pp. 332–346.
- [10] M. Ishii and T. Hibiki. *Thermo-Fluid Dynamics of Two-Phase Flow*. New York, NY: Springer New York, 2011.
- [11] D. A. Drew. “Mathematical Modeling of Two-Phase Flow”. In: *Annual Review of Fluid Mechanics* 15.1 (1983), pp. 261–291.
- [12] K. A. Pericleous and S. N. Drake. “An Algebraic Slip Model of PHOENICS for Multi-phase Applications”. In: *Numerical Simulation of Fluid Flow and Heat/Mass Transfer Processes*. Ed. by N. C. Markatos, M. Cross, D. G. Tatchell, and N. Rhodes. Vol. 18. Berlin, Heidelberg: Springer Berlin Heidelberg, 1986, pp. 375–385.
- [13] N. Zuber and J. A. Findlay. “Average Volumetric Concentration in Two-Phase Flow Systems”. In: *Journal of Heat Transfer* 87.4 (1965), pp. 453–468.
- [14] M. Manninen, V. Taivassalo, and S. Kallio. *On the Mixture Model for Multiphase Flow*. VTT Publications 288. Espoo: Technical Research Centre of Finland, 1996.
- [15] M. Ungarish. *Hydrodynamics of Suspensions*. Berlin, Heidelberg: Springer Berlin Heidelberg, 1993.
- [16] S. Johansen, N. Anderson, and S. De Silva. “A Two-Phase Model for Particle Local Equilibrium Applied to Air Classification of Powders”. In: *Powder Technology* 63.2 (1990), pp. 121–132.
- [17] B. Thomases and M. Shelley. “Emergence of Singular Structures in Oldroyd-B Fluids”. In: *Physics of Fluids* 19.10 (2007), p. 103103.
- [18] J. Du, D. Kim, G. Alhawaal, D. N. Ku, and A. L. Fogelson. “Clot Permeability, Agonist Transport, and Platelet Binding Kinetics in Arterial Thrombosis”. In: *Biophysical Journal* 119.10 (2020), pp. 2102–2115.
- [19] G. L. Celora, M. G. Hennessy, A. Muench, B. Wagner, and S. Waters. “The Dynamics of a Collapsing Polyelectrolyte Gel”. In: *SIAM Journal on Applied Mathematics* 83.3 (2023), pp. 1146–1171.
- [20] M. Aggarwal, N. G. Cogan, and O. L. Lewis. “Physiological Insights into Electrodiffusive Maintenance of Gastric Mucus through Sensitivity Analysis and Simulations”. In: *Journal of Mathematical Biology* 83.3 (2021), p. 30.
- [21] C. Serrano, P. R. Harris, P. D. Smith, and D. Bimczok. “Interactions between H. Pylori and the Gastric Microbiome: Impact on Gastric Homeostasis and Disease”. In: *Current Opinion in Physiology* 21 (2021), pp. 57–64.
- [22] C. Su, M. Padra, M. A. Constantino, S. Sharba, A. Thorell, S. K. Lindén, and R. Bansil. “Influence of the Viscosity of Healthy and Diseased Human Mucins on the Motility of Helicobacter Pylori”. In: *Scientific Reports* 8.1 (2018), p. 9710.

- [23] M. J. Berger and J. Oliger. “Adaptive mesh refinement for hyperbolic partial differential equations”. In: *Journal of Computational Physics* 53.3 (1984), pp. 484–512.
- [24] M. Berger and P. Colella. “Local Adaptive Mesh Refinement for Shock Hydrodynamics”. In: *Journal of Computational Physics* 82.1 (1989), pp. 64–84.
- [25] A. Dubey, A. Almgren, J. Bell, M. Berzins, S. Brandt, G. Bryan, P. Colella, D. Graves, M. Lijewski, F. Löffler, B. O’Shea, E. Schnetter, B. Van Straalen, and K. Weide. “A Survey of High Level Frameworks in Block-Structured Adaptive Mesh Refinement Packages”. In: *Journal of Parallel and Distributed Computing* 74.12 (2014), pp. 3217–3227.
- [26] C. Burstedde, L. C. Wilcox, and O. Ghattas. “P4est : Scalable Algorithms for Parallel Adaptive Mesh Refinement on Forests of Octrees”. In: *SIAM Journal on Scientific Computing* 33.3 (2011), pp. 1103–1133.
- [27] O. S. Lawlor, S. Chakravorty, T. L. Wilmarth, N. Choudhury, I. Dooley, G. Zheng, and L. V. Kalé. “ParFUM: A Parallel Framework for Unstructured Meshes for Scalable Dynamic Physics Applications”. In: *Engineering with Computers* 22.3-4 (2006), pp. 215–235.
- [28] J. B. Bell, P. Colella, and H. M. Glaz. “A Second-Order Projection Method for the Incompressible Navier-Stokes Equations”. In: *Journal of Computational Physics* 85.2 (1989), pp. 257–283.
- [29] J. Kim and P. Moin. “Application of a Fractional-Step Method to Incompressible Navier-Stokes Equations”. In: *Journal of Computational Physics* 59.2 (1985), pp. 308–323.
- [30] J. Van Kan. “A Second-Order Accurate Pressure-Correction Scheme for Viscous Incompressible Flow”. In: *SIAM Journal on Scientific and Statistical Computing* 7.3 (1986), pp. 870–891.
- [31] B. E. Griffith. “An Accurate and Efficient Method for the Incompressible Navier-Stokes Equations Using the Projection Method as a Preconditioner”. In: *Journal of Computational Physics* 228.20 (2009), pp. 7565–7595.
- [32] J. P. Keener, S. Sircar, and A. L. Fogelson. “Kinetics of Swelling Gels”. In: *SIAM Journal on Applied Mathematics* 71.3 (2011), pp. 854–875.
- [33] G. B. Wright, R. D. Guy, and A. L. Fogelson. “An Efficient and Robust Method for Simulating Two-Phase Gel Dynamics”. In: *SIAM Journal on Scientific Computing* 30.5 (2008), pp. 2535–2565.
- [34] A. Barrett. “An Adaptive Viscoelastic Fluid Solver: Formulation, Verification, and Applications to Fluid-Structure Interaction”. PhD thesis. The University of North Carolina at Chapel Hill University Libraries, 2019.
- [35] R. D. Guy and A. L. Fogelson. “A Wave Propagation Algorithm for Viscoelastic Fluids with Spatially and Temporally Varying Properties”. In: *Computer Methods in Applied Mechanics and Engineering* 197.25-28 (2008), pp. 2250–2264.
- [36] *IBAMR: An Adaptive and Distributed-Memory Parallel Implementation of the Immersed Boundary Method*. <https://github.com/IBAMR/IBAMR>.
- [37] R. D. Hornung and S. R. Kohn. “Managing Application Complexity in the SAMRAI Object-Oriented Framework”. In: *Concurrency and Computation: Practice and Experience* 14.5 (2002), pp. 347–368.
- [38] S. Balay, W. Gropp, L. C. McInnes, and B. F. Smith. “PETSc, the portable, extensible toolkit for scientific computation”. In: *Argonne National Laboratory* 2.17 (1998).
- [39] B. E. Griffith. “Immersed Boundary Model of Aortic Heart Valve Dynamics with Physiological Driving and Loading Conditions”. In: *International Journal for Numerical Methods in Biomedical Engineering* 28.3 (2012), pp. 317–345.
- [40] P. L. Roe and M. J. Baines. *Algorithms for Advection and Shock Problems*. 1982, pp. 281–290.

- [41] W. L. Briggs, V. E. Henson, and S. F. McCormick. *A Multigrid Tutorial, Second Edition*. Second. Society for Industrial and Applied Mathematics, 2000.
- [42] T. V. Gerya, D. A. May, and T. Duretz. “An Adaptive Staggered Grid Finite Difference Method for Modeling Geodynamic Stokes Flows with Strongly Variable Viscosity”. In: *Geochemistry, Geophysics, Geosystems* 14.4 (2013), pp. 1200–1225.
- [43] G. I. Taylor. “The Formation of Emulsions in Definable Fields of Flow”. In: *Proceedings of the Royal Society of London. Series A, Containing Papers of a Mathematical and Physical Character* 146.858 (1934), pp. 501–523.
- [44] B. Thomases and M. Shelley. “Transition to Mixing and Oscillations in a Stokesian Viscoelastic Flow”. In: *Physical Review Letters* 103.9 (2009), p. 094501.

A Appendix

A.1 Box relaxation solver

We define the operators $\mathcal{L}^h[\theta]$, \mathcal{C}^h , and $\mathcal{G}^h[\theta]$ that appear in the linear system (see equation (36)) for the box relaxation solver below:

$$\mathcal{L}^h[\theta] = \begin{bmatrix} -\frac{\theta_{i,j}+\theta_{i-1,j}}{h^2} - \frac{\theta_{i-\frac{1}{2},j+\frac{1}{2}}+\theta_{i-\frac{1}{2},j-\frac{1}{2}}}{\Delta y^2} & \frac{\theta_{i,j}}{\Delta x^2} & -\frac{\theta_{i-\frac{1}{2},j-\frac{1}{2}}-\theta_{i,j}}{\Delta x\Delta y} & \frac{\theta_{i-\frac{1}{2},j+\frac{1}{2}}-\theta_{i,j}}{\Delta x\Delta y} \\ \frac{\theta_{i,j}}{\Delta x^2} & -\frac{\theta_{i+1,j}+\theta_{i,j}}{\Delta x^2} - \frac{\theta_{i+\frac{1}{2},j+\frac{1}{2}}+\theta_{i+\frac{1}{2},j-\frac{1}{2}}}{\Delta y^2} & \frac{\theta_{i+\frac{1}{2},j-\frac{1}{2}}+\theta_{i,j}}{\Delta x\Delta y} & -\frac{\theta_{i+\frac{1}{2},j+\frac{1}{2}}-\theta_{i,j}}{\Delta x\Delta y} \\ \frac{\theta_{i-\frac{1}{2},j+\frac{1}{2}}-\theta_{i,j}}{\Delta x\Delta y} & -\frac{\theta_{i+\frac{1}{2},j+\frac{1}{2}}+\theta_{i,j}}{\Delta x\Delta y} & \frac{\theta_{i,j}}{\Delta y^2} & -\frac{\theta_{i,j+1}+\theta_{i,j}}{\Delta y^2} - \frac{\theta_{i+\frac{1}{2},j+\frac{1}{2}}+\theta_{i-\frac{1}{2},j+\frac{1}{2}}}{\Delta x^2} \\ -\frac{\theta_{i-\frac{1}{2},j-\frac{1}{2}}-\theta_{i,j}}{\Delta x\Delta y} & \frac{\theta_{i+\frac{1}{2},j-\frac{1}{2}}-\theta_{i,j}}{\Delta x\Delta y} & -\frac{\theta_{i,j}-\theta_{i,j-1}}{\Delta y^2} - \frac{\theta_{i+\frac{1}{2},j-\frac{1}{2}}+\theta_{i-\frac{1}{2},j-\frac{1}{2}}}{\Delta x^2} & \frac{\theta_{i,j}}{\Delta y^2} \end{bmatrix}, \quad (47)$$

$$\mathcal{C}^h = \begin{bmatrix} \theta_{n_{i-\frac{1}{2},j}}\theta_{s_{i-\frac{1}{2},j}} & 0 & 0 & 0 \\ 0 & \theta_{n_{i+\frac{1}{2},j}}\theta_{s_{i+\frac{1}{2},j}} & 0 & 0 \\ 0 & 0 & \theta_{n_{i,j-\frac{1}{2}}}\theta_{s_{i,j-\frac{1}{2}}} & 0 \\ 0 & 0 & 0 & \theta_{n_{i,j+\frac{1}{2}}}\theta_{s_{i,j+\frac{1}{2}}} \end{bmatrix}, \quad (48)$$

$$\mathcal{G}^h[\theta] = \begin{bmatrix} -\theta_{i-\frac{1}{2},j} & \theta_{i+\frac{1}{2},j} & -\theta_{i,j-\frac{1}{2}} & \theta_{i,j+\frac{1}{2}} \end{bmatrix}^T, \quad (49)$$

and

$$b[\theta, \mathbf{u}] = \begin{bmatrix} -\frac{\theta_{i-1,j}u_{i-\frac{3}{2},j}}{\Delta x^2} - \frac{\theta_{i-\frac{1}{2},j-\frac{1}{2}}u_{i-\frac{1}{2},j+1}}{\Delta y^2} - \frac{\theta_{i-\frac{1}{2},j-\frac{1}{2}}u_{i-\frac{1}{2},j-1}}{\Delta y^2} + u_{i-1,j+\frac{1}{2}}\frac{\theta_{i-\frac{1}{2},j+\frac{1}{2}}-\theta_{i-1,j}}{\Delta x\Delta y} - u_{i-1,j-\frac{1}{2}}\frac{\theta_{i-\frac{1}{2},j-\frac{1}{2}}-\theta_{i-1,j}}{\Delta x\Delta y} - \frac{\theta_{i-\frac{1}{2},j}p_{i-1,j}}{\mu\Delta x} \\ -\frac{\theta_{i+1,j}u_{i+\frac{3}{2},j}}{\Delta x^2} - \frac{\theta_{i+\frac{1}{2},j+\frac{1}{2}}u_{i+\frac{1}{2},j+1}}{\Delta y^2} - \frac{\theta_{i+\frac{1}{2},j-\frac{1}{2}}u_{i+\frac{1}{2},j-1}}{\Delta y^2} - u_{i+1,j+\frac{1}{2}}\frac{\theta_{i+\frac{1}{2},j+\frac{1}{2}}-\theta_{i+1,j}}{\Delta x\Delta y} + u_{i+1,j-\frac{1}{2}}\frac{\theta_{i+\frac{1}{2},j-\frac{1}{2}}-\theta_{i+1,j}}{\Delta x\Delta y} + \frac{\theta_{i+\frac{1}{2},j}p_{i+1,j}}{\mu\Delta x} \\ -\frac{\theta_{i,j+1}v_{i,j+\frac{3}{2}}}{\Delta y^2} - \frac{\theta_{i+\frac{1}{2},j+\frac{1}{2}}v_{i+1,j+\frac{1}{2}}}{\Delta x^2} - \frac{\theta_{i-\frac{1}{2},j+\frac{1}{2}}v_{i-1,j+\frac{1}{2}}}{\Delta x^2} - u_{i+\frac{1}{2},j+1}\frac{\theta_{i+\frac{1}{2},j+\frac{1}{2}}-\theta_{i,j+1}}{\Delta x\Delta y} + u_{i-\frac{1}{2},j+1}\frac{\theta_{i-\frac{1}{2},j+\frac{1}{2}}-\theta_{i,j+1}}{\Delta x\Delta y} + \frac{\theta_{i,j+\frac{1}{2}}p_{i,j+1}}{\mu\Delta y} \\ -\frac{\theta_{i,j-1}v_{i,j-\frac{3}{2}}}{\Delta y^2} - \frac{\theta_{i+\frac{1}{2},j-\frac{1}{2}}v_{i+1,j-\frac{1}{2}}}{\Delta x^2} - \frac{\theta_{i-\frac{1}{2},j-\frac{1}{2}}v_{i-1,j-\frac{1}{2}}}{\Delta x^2} + u_{i+\frac{1}{2},j-1}\frac{\theta_{i+\frac{1}{2},j-\frac{1}{2}}-\theta_{i,j-1}}{\Delta x\Delta y} - u_{i-\frac{1}{2},j-1}\frac{\theta_{i-\frac{1}{2},j-\frac{1}{2}}-\theta_{i,j-1}}{\Delta x\Delta y} - \frac{\theta_{i,j-\frac{1}{2}}p_{i,j-1}}{\mu\Delta y} \end{bmatrix}. \quad (50)$$